Argonne NATIONAL LABORATORY

ANL-GenIV-049

Scalability of the Natural Convection Shutdown Heat Removal Test Facility (NSTF) Data to VHTR/NGNP RCCS Designs

Nuclear Engineering Division

About Argonne National Laboratory

Argonne is a U.S. Department of Energy laboratory managed by UChicago Argonne, LLC under contract DE-AC02-06CH11357. The Laboratory's main facility is outside Chicago, at 9700 South Cass Avenue, Argonne, Illinois 60439. For information about Argonne, see www.anl.gov.

Availability of This Report

This report is available, at no cost, at http://www.osti.gov/bridge. It is also available on paper to the U.S. Department of Energy and its contractors, for a processing fee, from:

U.S. Department of Energy
Office of Scientific and Technical Information
P.O. Box 62
Oak Ridge, TN 37831-0062
phone (865) 576-8401
fax (865) 576-5728
reports@adonis.osti.gov

ANL-GenIV-049

Scalability of the Natural Convection Shutdown Heat Removal Test Facility (NSTF) Data to VHTR/NGNP RCCS Designs

by
R.B. Vilim and E.E. Feldman
Nuclear Engineering Division, Argonne National Laboratory

June 30, 2005

work sponsored by

U. S. Department of Energy,
Office of Nuclear Energy, Science and Technology

TABLE OF CONTENTS

List of Figures

List of Figures (continued)

List of Tables

SCALABILITY OF THE NATURAL CONVECTION SHUTDOWN HEAT REMOVAL TEST FACILITY (NSTF) DATA TO VHTR/NGNP RCCS DESIGNS

ABSTRACT

Passive safety in the Very High Temperature Reactor (VHTR) is strongly dependent on the thermal performance of the Reactor Cavity Cooling System (RCCS). Scaled experiments performed in the Natural Shutdown Test Facility (NSTF) are to provide data for assessing and/or improving computer code models for RCCS phenomena. Design studies and safety analyses that are to support licensing of the VHTR will rely on these models to achieve a high degree of certainty in predicted design heat removal rate. To guide in the selection and development of an appropriate set of experiments a scaling analysis has been performed for the air-cooled RCCS option. The goals were to 1) determine the phenomena that dominate the behavior of the RCCS, 2) determine the general conditions that must be met so that these phenomena and their relative importance are preserved in the experiments, 3) identify constraints specific to the NSTF that potentially might prevent exact similitude, and 4) then to indicate how the experiments can be scaled to prevent distortions in the phenomena of interest.

The phenomena identified as important to RCCS operation were also the subject of a recent PIRT study. That work and the present work collectively indicate that the main phenomena influencing RCCS heat removal capability are 1) radiation heat transport from the vessel to the air ducts, 2) the integral effects of momentum and heat transfer in the air duct, 3) buoyancy at the wall inside the air duct giving rise to mixed convection, and 4) multidimensional effects inside the air duct caused by non-uniform circumferential heat flux and non-circular geometry.

The NSTF provides a capability for full-scale experiments in all but two geometric dimensions. The dimensions are 1) the distance from the vessel surface to the front of the duct face and 2) the length of the heated section. The scaling analysis showed, nevertheless, that similitude can be preserved for the above four phenomena on an individual basis if they are regarded as separate effects. Furthermore, the distribution of heating on the duct faces is not affected by (1). The heat flow into the test section and the air duct loss coefficient provide two independent degrees of freedom and can be used to tailor experiment conditions to achieve similitude in each instance. Additionally, by introducing further degrees of freedom, such as the duct aspect ratio and the distance between ducts, it may be possible to achieve similitude for more than one of these separate effects simultaneously in a single experiment. This is left as a task for the next phase of the project which is to produce an experiment test plan in conjunction with the refurbishment of the facility. This is in preparation for the performance of VHTR-focused experiments in the NSTF.

Review of the current NSTF database accumulated from past experiments performed for the IFR program indicates that from the scaling perspective, more than half of the 71 unfinned experiments performed are in the mixed convection region, the region where the

RCCS air duct is expected to operate. Thus, while the data indicate exact scaling of the Reynolds and Grashof numbers between the NSTF and the RCCS is not achieved in the duct interior, the mixed convection phenomenon is preserved. The NSTF data offer an opportunity to validate CFD codes in the mixed convection region for Reynolds numbers between 37,700 and 170,000 and Grashof numbers between $8x10^8$ and $3.5x10^9$. Some extrapolation would be required to analyze the RCCS air duct at a Reynolds number of 14,000 and Grashof number of 10^7 where it is expected to operate. However, since the convection mode remains the same, if a single set of turbulence parameters give consistent predictive behavior over the range of NSTF data, we might have confidence in extrapolating down to RCCS conditions.

I. INTRODUCTION

The Very High Temperature Gas Reactor (VHTR) exhibits essentially walk-away safety for even the most severe design basis events. In the event of loss of all active cooling systems and depressurization of the primary system, a passive cooling system is designed to maintain core temperatures within safe limits. No actions on the part of the operator are needed. Shutdown heat is conducted radially from the inner core out to the reactor vessel wall where it is then radiated to a natural draft cooling system. A combination of relatively low core power density and an annular shaped core limit the radial temperature rise across the core. The natural draft system limits vessel temperature. These features coupled with a high fuel temperature capability provide a wide margin to fuel failure.

The natural draft cooling system is an important element in the overall safety of the VHTR. As the ultimate heat sink the plant designer must be able to reliably predict its heat removal capability. Testing of full scale prototypes is expensive and does not permit timely study of design options. Instead, the vendor will perform these design studies using combinations of a 1-D integrated systems code and a CFD code to simulate actual behavior. This of course requires that the codes be properly qualified including a measure of the uncertainty in predictive capability obtained by comparison with experiment data. Performing these code assessment activities using published data is not feasible. The draft chimney heat removal system involves a combination of factors that collectively give rise to a unique case that is not found within the body of experiments reported in the engineering literature. These include non-uniform wall heat flux in a rectangular duct geometry, radiation heat transport among the walls within the duct, mixed convection heat transfer in a rectangular duct geometry, and a large variation in fluid properties in the axial direction, particularly viscosity. Thus, there is a need for a select set of scaled experiments in which the phenomena important to draft cooling system operation figure prominently. These tests are to be performed at Argonne National Laboratory in the Natural Convection Shutdown Heat Removal Test Facility (NSTF).

Several factors are relevant in the selection of an appropriate set of experiments and related modifications of the NSTF. The facility may not necessarily be full scale yet one must be certain that important phenomena are present and without distortion. There may be a range of operating conditions and geometries that must be characterized leading to a potentially large number of experiments.

A scaling analysis is an effective means of dealing with these issues. It provides a means of identifying the phenomena that are important to air draft cooling system operation and of ensuring that these phenomena are properly represented in the experiments to be performed in the test facility. It also provides a means for identifying a canonical set of experiments that yield the needed data and result in a more manageable number of experiments. In addition a scaling analysis often renders the trend of an important safety variable with a change in an independent variable (e.g., experiment heated length) and the underlying basis for the trend more apparent compared with a parametric analysis performed with a CFD code.

II. HEAT REMOVAL CONCEPTS

There are three vendors developing gas reactor VHTR designs. The General Atomics (GA) design is based on the lower temperature GT-MHR and employs an air-cooled Reactor Cavity Cooling System (RCCS). The AREVA design is the ANTARES plant and at this point appears to be a water-cooled conceptual design. [1] The South African/ Westinghouse design is water cooled. In this report we examine the air-cooled RCCS and leave the water cooled design for FY2006.

The RCCS for the GT-MHR is shown in Figures 1 through 5 which are taken from [2]. A schematic representation of the flow of decay heat from the reactor vessel to the RCCS air flow appears in Figure 1. Heat from the reactor vessel is transferred by radiation and natural convection to the outer surface of the duct carrying the RCCS air flow. The air flow through the RCCS ducts is outside air that is driven entirely by natural convection. Outside air enters and travels downwards inside ductwork to the bottom of the reactor cavity, as shown by the solid black arrows. The air then makes a U-turn and travels upwards through cooling panels and ultimately exits through outlet chimneys. The air while traveling through the RCCS cooling panels picks up heat that was transferred through the walls of these panels. This heat gradually heats the air, as shown by a progression of lighter arrows in the figure. The ductwork and cooling panels keep the outside air, which is used for cooling, separate from the air that is trapped inside the reactor cavity. The figure also shows the conduction/radiation and natural circulation paths used to transfer the heat from the central regions of the reactor to the reactor vessel wall.

Figure 2 provides additional details on the air flow paths in the RCCS ductwork. Inlet and outlet ducts tend to occur in concentric pairs with the hot exit air at the center of the cold inlet air. However, heat transfer between adjacent hot and cold streams should be minimized in order to maximize gravity heads and in order to deliver the coldest air to the cooling panels where it can do the most good. There are multiple sets of these hot and cold pairs and they join at common headers and then divide again into multiple paths. This approach is used so that if a duct gets blocked, the remaining parallel paths are able to transport the required flow.

Figure 3 shows that separate compartments in the reactor building are used for the reactor vessel and the power conversion unit. The RCCS cooling panels and a bottom cold plenum for the air are shown in the compartment that contains the reactor vessel. The locations of some of the concentric air ductwork are also indicated in the figure. The inlet/outlet structure for the air flow is shown at the top.

Figures 4 and 5 provide elevation and top views, respectively, of the reactor compartment in the reactor building. The location of the cooling panels is of particular interest. In Figure 4 the “hot risers” are the cooling panels. As Figure 4 shows, these traverse the most of the reactor vessel height. In Figure 5 the cooling panels are not labeled, but they can be observed are running along the perimeter of the wall of the compartment. There should be 292 of these 2-inch by 10-inch panels.

III. PHENOMENA IN THE RCCS

The phenomena of interest in a scaling analysis are those that dominate RCCS behavior and thus have a bearing on whether the design objective will be met. The design goal is safe removal of decay heat during those accidents where all other heat removal systems are inoperable. A recent PIRT study [3] found that the important phenomena occur in two components of the RCCS, the reactor cavity and the air duct. The important phenomena in each of these components are summarized below.

Within the reactor cavity, heat is transferred from the vessel wall to the air ducts mainly by radiation heat transfer. Computer code calculations with CFD models indicate that this is 90 percent of the heat transfer with convection from natural circulation patterns set up in the reactor cavity making up the balance.[4] The reactor vessel height is about 20 times the average thickness of the cavity and the temperature drop radially across the cavity is greater than 200C so the dominant direction of heat transfer is horizontal. The view factors between vessel and air duct are especially complicated functions of geometry. The vessel is cylindrical while the ducts and their placement in the cavity are on a Cartesian grid. Radiation heat transport in this mixed geometry is best modeled with a CFD code.

Within the air duct, radiant energy incident on the exterior walls is conducted through the walls to the interior surfaces where it heats the air by convection. Energy is also radiated from the interior surfaces and is incident on adjacent surfaces. A buoyant head is established inside the duct as the air is heated, expands, rises, and exits the stack with cold air drawn in at the duct inlet. The convective heat transfer and friction pressure drop processes inside the duct are dependant on the velocity profile at the wall. If local buoyancy at the wall is present, then the heat transfer and friction pressure loss processes operate in the mixed rather than forced convection region. Because of the non-circular geometry of the duct and non-uniform circumferential heat flux, representation of these processes requires geometric parameters different from those used to describe flow in a circular vertical heated channel.

IV. DESIGN CONDITIONS

A. Design Basis Events

The RCCS is designed to provide passive cooling of the reactor for events for which all active heat removal systems are inoperable. It must be sized to safely limit temperatures for the associated plant conditions. To determine these conditions it is helpful note that the relevant event initiators are a subset of the spectrum of possible equipment failures and/or operator errors. The spectrum is subsumed by seven event classes: reactivity insertion, loss of heat sink, loss of flow, overcooling, flow runup, flow blockage, and loss of coolant. In each class there is a single event that bounds the severity of conditions for all events in the class. These worst case single events give rise to a plant transient that can be broken into a sequence of transient phases. It is in these transient

phases that the design requirements for RCCS performance become apparent. The transient phases are identified by examining what key features describe the thermal-hydraulic regime the reactor is operating in. This is a function of three variables: pressure, cooling mode, and heating mode. As shown in Figure 6, for these variables, respectively: the reactor is pressurized or depressurized; there is net flow through the core or there is only internal re-circulation; and the core is neutronically critical or is shutdown and producing decay heat. Table 1 gives the values of these features for all classes of duty cycle, design basis, and beyond design basis events. Table 2 rearranges this information giving the event classes in each operating regime.

The reactor transient phases that the RCCS must be designed for are those in which conduction cooling rather than forced convection is used to cool the fuel and the vessel. Under such conditions all of the heat generated by the reactor must be removed by the RCCS. Thus, the events in Table 2 of greatest concern are the six events that rely on conduction cooling. The three unprotected events that rely on conduction cooling are beyond the design basis. Therefore, we focus on the other three, which are in OR3 and OR6 of Table 2. OR3 is a pressurized conduction cooldown (PCC) in which the pressure boundary is not breached but the loss of forced flow in the primary circuit causes the pressure to equilibrate throughout the circuit. The equilibrium pressure is governed by the volume of the circuit and the mass of helium in the circuit and its average temperature. OR6 is a depressurized conduction cooldown (DCC) and is similar to OR3 in that there is a loss of forced flow. The pressure also equilibrates throughout the primary circuit, but the pressure boundary is breached and causes the final pressure to reduce to atmospheric pressure instead of the 50 bars of the pressurized case.

B. Performance Variations

Among the phenomena of concern with regard to the performance of the RCCS are 1) the heat transfer from the inner surfaces of the cooling ducts in the RCCS to the air flowing inside the ducts (described in the next section) and 2) the air flow rate in the RCCS ducts, which is governed by the hydraulic resistances in the RCCS air flow circuit. The predictions of the model depend on values of parameters that are used in the representation of these phenomena. Therefore, for both the PCC and the DCC, key parameters in the RELAP5/ATHENA model were varied to study the sensitivity of the RCCS conditions to variations in these parameters due either to design variations or uncertainties in the RELAP5/ATHENA modeling. INL provided a RELAP5/ATHENA model, including the input for the two upset transients being considered. For both the PCC and the DCC transients, four cases were analyzed in the studies. These cases are:

1. Base Case
   This is the model as provide by INL.

2. 80% RCCS Inner Surface Film Coefficient
   This is the Base Case with the film coefficient on the inner surfaces of the RCCS coolant ducts reduced by 20%. This was accomplished in the model by reducing the fouling factor inside the RCCS ducts from 1.0 to 0.8.

3. 50% Inner Surface Film Coefficient
   This is the Base Case with the film coefficient on the inner surfaces of the RCCS coolant ducts reduced by 50%.

4. 80.12% air flow in RCCS
   This is the Base Case with the initial air flow rate reduce to 80.12% of that for the Base Case. This flow reduction was accomplished by doubling three of the K-losses in the RCCS air flow path model. These three are at the inlet and the outlet to ducts (node 970 in Figure 7) and between nodes 975 and 980 in Figure 7.

The Base Case was analyzed to provide a reference with which all of the others could be compared. It was observed that peaks in fuel and reactor vessel temperature tend to occur gradually and typically within the first four days after shutdown. Therefore, all cased were designed to simulate the first four days of the transient.

The transient result for the PCC cases are provided in Figures 8 through 11. In the legends of these figures, "20% Reduction" refers to Case 2 and "50% Reduction" refers to Case 3. Figure 8 provides peak fuel temperature, Figure 9 provides peak reactor vessel temperature, Figure 10 provides the RCCS exit coolant temperature, and Figure 11 provides the power removed by the air in flowing through the RCCS ducts. The power removed was calculated from the instantaneous air inlet and outlet temperatures and flow rate. These four figures compare Cases 2 through 4 with the Base Case. In each of these figures the curves appear in the same order that they are shown in the legend. The transient results of the DCC cases are provided in Figures 12 through 15 and are arranged in an analogous manner to their PCC counterparts. In the two figures showing RCCS power, Figures 11 and 15, the Base Case curve and the 20% film coefficient reduction curve are nearly coincident, as are the 50% film coefficient reduction curve and the 80.12% flow curve.

Each peak fuel or vessel curve represents a temperature history at a single point in the reactor. The location of the peak fuel temperature and the location of the peak vessel temperature were obtained by surveying all candidate locations for the maximum. Then only the temperatures at these locations were plotted. Thus, if the location of the peak changes with time, higher values than those shown could be observed for all but the absolute peak. The peak vessel temperatures occur on the inner surface of the vessel because the heat source is inside the vessel. A substantial temperature gradient across the vessel wall thickness it to be expected. It is important to keep the temperature drop across the reactor vessel in mind when interpreting the results because it is the temperature on the outer surface of the vessel that determines the behavior of the RCCS. Similarly, the axial distribution along this surface is important because the entire surface provides the energy that is removed by the RCCS.

Table 3 provides a summary of the peak fuel and vessel temperatures for the PCC. The maximum and minimum air flow rates for the RCCS are also included in the table.

Table 4 provides analogous results to Table 3, but for the DCC. These results show that variations in RCCS air flow rate are small within each case and that air flow rate is only slightly affected by the RCCS film coefficient or whether a PCC or a DCC is being considered.

As far as the safety criteria are concerned, for the variations in parameter ranges allowed in this investigation, none of the cases lead to very large perturbations in either peak fuel or vessel temperatures. The reduced RCCS duct film coefficient has only a very minor effect on the peak fuel temperatures – no more than about 6º C increase – and no more than about a 23º C increase in peak vessel temperature for the cases studied. Halving the film coefficient should cause an approximate doubling of the film temperature rise between the mixed-mean temperature of the flowing air in the RCCS duct and the duct inner surface. This should cause a corresponding increase in the temperature on the outer surface of the RCCS duct. Since the mode of heat transfer between the this surface and the outer surface of the reactor vessel is by radiation, which correlates with a difference in the forth powers of absolute temperature of the two surfaces, the increase in the temperature on the outer surface of the vessel should be much less than the increase in the film temperature inside the RCCS duct. If steady-state or nearly state-state heat transfer were occurring when the peak fuel temperature was approached an increase in vessel temperature would results in a nearly equal increase in fuel temperature. However, a higher peak fuel temperature allows more heat to be stored as the higher peak is approached and this causes the increase in the peak fuel temperature to be diminished and therefore be considerably less than the increase in the reactor vessel temperature.

Reducing the RCCS air flow rate has a similar effect on peak fuel and reactor vessel temperatures as does reducing the RCCS duct film coefficient in that both concepts impede heat transfer through the RCCS. The peak fuel and vessel temperatures for the nearly 20% reduction in RCCS air flow rate tend to fall between those for the 20% and 50% reduction in RCCS film coefficient. From this perspective the variation in RCCS conditions obtained from these parametrics could form the basis for the follow-on scaling studies.

As Figures 10 and 14 shows, reducing the RCCS air flow by nearly 20% causes about a 30º C increase in the RCCS air outlet temperature during the two accidents. On the contrary, the changes in the air film heat transfer coefficient within the duct have a minor effect on the duct air coolant outlet temperature. There are natural compensating feedback effects. The RCCS conditions change insignificantly. Both Tables 3 and 4 show that the resultant air flow in the cases 2 and 3 are also very close to the results form the base case, case 1. This is a further indication of compensating effects. Changes in the form losses in the RCCS though is a different feedback scenario as evidenced by the results of case 4. However, as Figures 11 and 15 show, the power removed by the air flowing through the RCCS is relatively insensitive to both the RCCS film coefficient or the flow rate. Although there is as much as about a 10% difference in power removal close to the initiation of the transient, at the time where the peak fuel and vessel

temperatures occur, beyond 40 hours in all instances, the differences in power removal are small. All the cases start off at the same initial steady state conditions.

V. THE APPROACH TO SCALING ANALYSIS

The basic goal of a scaling analysis is to determine or demonstrate how a scale model of a physical system can be used to study phenomenon occurring in the latter. The approach is based on the premise that if two dissimilar systems satisfy the same set of equations, either system can be used to model the other. [5] The scale model is referred to as the *experiment*; the physical system is the *plant*. Generally, the task is to determine the values of physical parameters in the experiment that permit it to be a surrogate for predicting plant behavior. That is the task addressed in this report. It can be broken into the five steps summarized as follows:

1. Develop model equations. It is assumed that the intent is to design the experiment to exhibit the same phenomenon important to operation of the plant. The same set of conservation equations and constitutive models for both the plant and experiment then represent the phenomena.

2. Non-dimensionalize model equations. The dependent and independent variables in the model equations are divided through by non-dimensionalizing scale factors and terms are collected. The result is a set of equations where the independent and dependant variables are dimensionless and the remaining terms in the equations are dimensionless groups that have an interpretation as ratios of magnitudes of physical phenomenon. Further, if the scaling is performed so that the dependent variables are O(1), then the magnitude of a dimensionless group compared to others provides a relative measure of its importance, i.e., the largest groups correspond to the most important phenomena.

3. State similarity conditions. If the experiment is to reflect the same important phenomena present in the plant, then the non-dimensionalized equations apply equally to the plant and experiment. To provide for this, one must choose parameter values in the experiment that reproduce the values the dimensionless groups take on in the plant. In this way the relative magnitudes of the phenomena with respect to each other are preserved. The similarity condition then is that for each dimensionless group, the ratio of the value in the experiment to that in the plant is unity. That is, $\Pi_R = \Pi_e / \Pi_p = 1$, where Π is a dimensionless group and subscripts *e*, *p*, *R* refer to experiment, plant, and ratio of experiment to plant, respectively.

4. Express the Π_R in terms of ratios of physical parameters. The Π_R can be expanded into ratios of the value of a parameter in the experiment to the value in the plant. Doing so provides a means for solving for experiment parameter values such that similarity between experiment and plant is preserved as in the next step.

5. Solve for the similarity conditions. The ratios of physical parameters in step 4 contain parameters whose values in the experiment are not known but are to be determined such that the similarity conditions are achieved. These parameters are treated as unknowns and each of the similarity conditions in step 3 provides an equation that must be satisfied. These equations are solved for the unknowns.

One issue in achieving similarity between the experiment and the plant involves the number of degrees of freedom in the experiment. Typically in a scaled experiment there are insufficient degrees of freedom to assure complete similarity. If this is the case, then a series of experiments can be conducted, each aimed at studying a subset of the phenomena. These individual experiments are referred to as *separate effect* experiments. Below we describe three experiments that address different phenomena should it not be possible to arrange for similarity among all three phenomena simultaneously in a single experiment.

In the RCCS the phenomena divide into those in the reactor cavity and those in the air duct. In the cavity the fraction of vessel energy going into each of the air duct faces should be preserved since this effects the temperature of each of the faces and in turn the overall radiative heat transfer capability of the cavity. It also results in a large asymmetry in circumferential heat flux at the wall inside the duct. This multidimensional effect may be important and should be the subject of an experiment. A scaling analysis is used to determine how the experiment geometry in the NSTF can be adjusted to preserve this heating split given that the distance from the vessel to front duct face in the NSTF is about 15% of the value in the plant.

Inside the air duct various scaling analyses are used identify the experiment conditions needed to preserve important phenomena. The integrated heat removal capability of the air duct is a factor in RCCS performance and should be the subject of an experiment. The heat removal capability is given by the simultaneous solution of the one-dimensional momentum equation for the air circuit and the fluid-energy equation for the heated section. In this experiment then similarity should be preserved with respect to these two equations. This must be achieved in the face of a heated length that is limited by the dimensions of the NSTF to about 65% of the value in the plant.

Internal buoyancy in the air duct is an important phenomenon that affects the radial velocity profile and hence the friction factor and hest transfer coefficients. It has a significant impact on safety related fuel and vessel temperatures as described earlier and should be the subject of an experiment. The experiment conditions for similarity are obtained from a Pi Theorem analysis of the important dimensional quantities.

VI. REACTOR CAVITY

A scaling analysis for the radiation component of heat transfer shows how the dimensions of the RCCS mock-up in the Natural Circulation Shutdown Test Facility

(NSTF) should be scaled to ensure that important dimensionless numbers are preserved in going from plant to experimental facility.

The scaling analysis adopts the RCCS design for the GT-MHR and assumes it is representative of the design for the VHTR. At this time the final design is not known. A plan view for the GT-MHR shows the reactor cavity is comprised of a single row of ducts arranged to form a square that is centered about a cylindrical reactor vessel. The backside of the ducts are displaced a short distance from the square cavity enclosure wall. This is shown in Figure 5.

The main features that appear in Figure 5 are abstracted into Figure 16 and are also assumed to appear in the NSTF mockup facility. At this time a geometrically exact and full scale facility is unwarranted given the uncertainty of the final RCCS design and the cost of such a facility. The geometry shown in Figure 16 is essentially a two-dimensional rendering of the GT-MHR design. The geometry preserves the orientation of ducts with respect to themselves and includes a planar heat source offset from the duct front faces and a planar back wall also offset from the ducts. It is assumed that the aspect ratio of the duct cross section and the distance between ducts can be freely varied within the NSTF. The distance from the vessel to the front faces of the duct is, however, constrained by the dimensions of the NSTF test section and will likely end up being not to geometric scale. The scaling analysis in this report addresses how this affects the proper placement of the ducts relative to the vessel face such that similitude for the powers into each face (front, side, and back is preserved).

A. Radiant Interchange

Heat transfer in the axial dimension will be ignored. The vessel is about 17 m high and the average distance from vessel to duct is about 0.8m and so this is a reasonable approximation. The heat flux at the vessel wall will be supplied as a boundary condition. Heat transfer by convection and conduction within the reactor cavity is ignored based on results in [4]. Figure 16 shows the geometry variables and Figure 17 the temperature variables used in the models developed below.

The surfaces in Figure 16 are assumed to be grey. That is, they do not absorb all the incident radiation as a black body would but reflect a fraction ρ. Further, the surfaces are assumed emit a fraction ε of the energy that a black body would at the same temperature. Here ρ is referred to as the reflectivity and ε as the emissivity. The total radiant energy leaving unit area of the ith surface is then

$$W_i = \varepsilon_i E_{bi} + \rho_i H_i \qquad (1)$$

where E_b is the energy flux emitted by a black body of the same temperature, and H is the incident radiant energy flux.

If surface i is one of n inside an enclosure, then the total radiant energy incident on surface i is

$$A_i H_i = W_1 A_1 F_{1i} + W_2 A_2 F_{2i} + ... + W_n A_n F_{ni} \quad (2)$$

where F_{ij} is the fraction of the radiant energy leaving surface j that is incident on surface i. One obtains by substituting the relations $A_i F_{ij} = A_j F_{ji}$ [6], $E_{bi} = \sigma T_i^4$ [6] and Eq. (2) into Eq. (1) the equation

$$W_i = \varepsilon_i \sigma T_i^4 + \rho_i \left(\sum_{j=1}^{n} W_j F_{ij} \right) \quad (3)$$

for surface i. Eq. (3) holds for each of the n surfaces. If the temperatures T_i are taken as boundary conditions, then we have n equations in the n unknowns W_i.

The *net* total energy flux leaving the surface is

$$q_i = W_i - H_i + q_{ci} = \frac{\varepsilon_i (E_{bi} - W_i)}{\rho_i} + q_{ci}. \quad (4)$$

where we have made use of Eq. (1), the relation $\varepsilon = 1 - \rho$ for a Gray body [6], and where q_{ci} is the convective heat flux component of q_i.

For the case where the net energy flux leaving a surface is the boundary condition rather than temperature, Eq. (3) is modified. Substituting the expression for $\varepsilon_i E_{bi}$ given by Eq. (4) into Eq. (3) gives

$$W_i = q_i + \left(\sum_{j=1}^{n} W_j F_{ij} \right) - q_{ci}. \quad (5)$$

B. View Factors

B.1 Single Duct within Reactor Cavity

There are five different surfaces within the enclosure formed by the vessel and downcomer. While there are ten view factors corresponding to the number of surface pairs, only half of these are independent. That is, view factors F_{ji} and F_{ij} are related through $A_j F_{ji} = Ai F_{ij}$. The five distinct pairs are vessel/side-of-duct (V-SD), side-of-duct/downcomer (SD-D), vessel/front-of-duct (V-FD), back-of-duct/downcomer (BD-D), and vessel/downcomer (V-D).

View factors for these were derived as follows. There are two surface pairs in Figure 16 that involve a simple obstruction, the reactor vessel as the source surface and

the side of the duct as the destination surface (V-SD) and the side of the duct as the source surface and the downcomer as the destination surface (SD-D). View factors for simple arrangements of two planes given in the literature and are combined to yield the view factors for V-SD and SD-D. Figure 18 shows the three elemental view factors from which a composite view factor can be assembled for V-SD. The first line entry in Table 5 shows how these elemental factors are combined to obtain the composite view factor $F_{V\text{-}SD}$. Similarly, Figure 19 shows the elemental factors from which a composite view factor can be assembled for SD-D. The third entry in Table 5 shows how these combine to form the composite factor $F_{SD\text{-}D}$. Surface pairs A-B, V-FD, and BD-D involve no obstructions as seen in Figures 18 and 20. Corresponding view factors F_{AB} , $F_{V\text{-}FD}$, and $F_{BD\text{-}D}$ each equal an elemental view factor shown in Table 5. The view factor for pair V-D is the fifth entry in Table 5 and is obtained through the relation

$$\sum_{i=1}^{n} F_{j-i} = 1 \tag{6}$$

where j = V. Composite reverse view factors are given in Table 6. Expressions for the elemental view factors in Table 5 are given in Table 7.

B.2 Extension to Infinite Array

The view factors derived above are for the exchange of radiant energy between the cavity walls and a single duct. In fact, for the infinite planar geometry we have assumed, the cavity walls are interacting with an infinite number of such ducts. If we seek view factors that represent the fraction of the total radiant energy from the vessel that lands on each of the different faces of the duct, then we must sum over all ducts. From Figure 16 the length of the array is $2l_\infty$. Each duct is a unit cell of length l_w+l_g. Hence, the number of ducts the vessel is interacting with is $2l_\infty / l_w+l_g$. Then the fraction of energy radiated by the vessel landing on the front faces of the ducts is

$$F_{V-FD} = \frac{2l_\infty}{l_w + l_g} F'_{V-FD} \tag{6a}$$

where the prime superscript is introduced to denote the view factor for a single duct. The fraction of the energy radiated by the vessel that is incident on the sides of the ducts is

$$F_{V-SD} = \frac{1}{2} F'_{V-SD} \frac{2l_\infty}{l_w + l_g} 2 \tag{6b}$$

where the first term on the right-hand side accounts for the fact that only one-half the energy radiated by the vessel has the chance of being seen by the face of one side of a duct, the second term represents the fraction of this energy that is actually incident on the face, the third term is the number of ducts, and the last term accounts for the fact that each duct has two sides. Similarly, view factors can be derived for the other pairs of duct faces interacting with the vessel and the downcomer.

B.3 Coupling to Interior of Duct

There are four different surfaces within the enclosure formed by the interior faces of the duct as shown in Figure 21. While there are twelve view factors corresponding to the number of surface pairs, only three of these are independent. That is, view factors F_{ji} and F_{ij} are related through $A_j F_{ji} = A_i F_{ij}$ and there is a symmetry axis. The three distinct pairs are side-of-duct interior /side-of-duct interior (SDI-SDI), front-of-duct interior/back-of-duct interior (FDI-BDI), and side-of-duct interior /back-of-duct interior (SDI/BDI). Composite view factors for the interior faces are given in Table 8. Elemental view factors used there are given in Table 9.

C. Equation Set

The thermal conductance of the duct wall will be lumped in with the heat transfer conductance between the bulk air inside the duct and the inner faces of the duct. Each of the inner faces has its own temperature.

The specific equation set that describes heat flow by radiation between the vessel wall, the downcomer wall, and the four faces of the duct is written. The radiation heat transfer between the faces within the duct is presently ignored. For the vessel with the heat flux as a boundary condition we have from Eq. (5)

$$W_V = q_V + W_{FD} F_{V-FD} + 2 W_{SD} F_{V-SD} + W_D F_{V-D} . \tag{7}$$

For the downcomer and the faces of the duct we have from Eq. (3),

$$W_D = \varepsilon_D \sigma T_D^4 + \rho_D \left(W_{BD} F_{D-BD} + 2 W_{SD} F_{D-SD} + W_V F_{D-V} \right) \tag{8}$$

$$W_{FD} = \varepsilon_{FD} \sigma T_{FD}^4 + \rho_{FD} W_V F_{FD-V} \tag{9}$$

$$W_{SD} = \varepsilon_{SD} \sigma T_{SD}^4 + \rho_{SD} \left(W_V F_{SD-V} + W_D F_{SD-D} \right) \tag{10}$$

$$W_{BD} = \varepsilon_{BD} \sigma T_{BD}^4 + \rho_{BD} W_D F_{BD-D} . \tag{11}$$

The net total energy flux out each of the outside faces of the duct is obtained from Eq. (4)

$$q_{FD} = \frac{\varepsilon_{FD}}{\rho_{FD}} \left(\sigma T_{FD}^4 - W_{FD} \right) , \tag{12}$$

$$q_{SD} = \frac{\varepsilon_{SD}}{\rho_{SD}} \left(\sigma T_{SD}^4 - W_{SD} \right) , \text{ and} \tag{13}$$

$$q_{BD} = \frac{\varepsilon_{BD}}{\rho_{BD}} \left(\sigma T_{BD}^4 - W_{BD} \right) . \tag{14}$$

For the interior of the duct we have from Eq. (3)

$$W_{FDI} = \varepsilon_{FDI}\,\sigma T_{FD}^{4} + \rho_{FDI}\left(W_{BDI}F_{FDI-BDI} + 2\,W_{SDI}F_{FDI-SDI}\right) \tag{15}$$

$$W_{SDI} = \varepsilon_{SDI}\,\sigma T_{SD}^{4} + \rho_{SDI}\left(W_{FDI}F_{SDI-FDI} + W_{BDI}F_{SDI-BDI}\right) \tag{16}$$

$$W_{BDI} = \varepsilon_{BD}\,\sigma T_{BD}^{4} + \rho_{BD}\left(W_{FDI}F_{BDI-FDI} + 2\,W_{SDI}F_{BDI\text{-}SDI}\right). \tag{17}$$

The net total energy flux out each of the inside faces of the duct is obtained from Eq. (4)

$$q_{FDI} = \frac{\varepsilon_{FD}}{\rho_{FD}}\left(\sigma T_{FD}^{4} - W_{FDI}\right) + h_{FDI}(T_{FDI} - T_C)\ , \tag{18}$$

$$q_{SD} = \frac{\varepsilon_{SD}}{\rho_{SD}}\left(\sigma T_{SD}^{4} - W_{SD}\right) + h_{SDI}(T_{SDI} - T_C)\text{, and} \tag{19}$$

$$q_{BD} = \frac{\varepsilon_{BD}}{\rho_{BD}}\left(\sigma T_{BD}^{4} - W_{BD}\right) + h_{BDI}(T_{BDI} - T_C)\,. \tag{20}$$

An energy balance on each of the duct faces gives

$$q_{FD} + q_{FDI} = 0\,, \tag{21}$$

$$q_{SD} + q_{SDI} = 0\,, \tag{22}$$

$$q_{BD} + q_{BDI} = 0\,, \tag{23}$$

where the bulk air is at temperature T_C and h is the convective heat transfer coefficient.

D. Similarity Conditions

As described in Section V, similarity conditions are sought that preserve important phenomena in going from plant to experiment. Accordingly, we seek for the reactor cavity the conditions that maintain the fraction of the total energy flow into each of the duct faces for reasons that are described in Section IX.

It is clear from the development of Eqs. (7) through (23) that the energy flow fractions depend on a number of factors. The vessel-duct face view factor is the most important as it represents the fraction of energy radiating from the vessel that is incident on a duct face. But other factors such as emissivity, vessel temperature, duct wall temperature, heat transfer coefficient at inner surface of duct, and air temperature also affect the energy flow split. However, if these other factors are maintained constant then Eqs.(7) through (23) show that the energy flow into the duct faces depends on only the

view factors. Assuming that these factors remain the same in going from plant to experiment, then the fraction of the total energy flow into each of the duct faces is preserved if the view factors are preserved.

VII. AIR DUCT

A scaling analysis for the air duct shows how the dimensions of the RCCS mock-up in the Natural Convection Shutdown Heat Removal Test Facility should be scaled to ensure that important dimensionless numbers are preserved in going from plant to experimental facility. The analysis assumes a natural circulation loop with the geometry shown in Figure 22. Heat is input at the bottom over a length l_h in a duct of overall length l_c. The coolant above the heated section is assumed to have density ρ_h while outside the duct the density is ρ_c . The time constants for heat flow to the vessel boundary during PCC and DCC are expected to be much longer than the time constant associated with the duct. Further, the RCCS is expected to be at temperature during normal operation so that there should be no startup transient. Thus, a quasi-static scaling analysis of the RCCS is adequate.

A. One-Dimensional Effects

A.1 Momentum Conservation

The momentum one-dimensional momentum balance in steady state equation is non-dimensionalized. We have,

$$\frac{\partial}{\partial z}\left(\frac{G^2}{\rho}\right) = -\frac{\partial P}{\partial z} - \frac{f\,G\,|G|}{2\,D_h\,\rho} - \rho\,g\cos\theta \tag{24}$$

where G is mass flux, ρ is density, P is pressure, f is friction factor, D_h is hydraulic diameter which is equal to four times the flow area divided by the wetted perimenter, and θ is the inclination angle. Integrating this around a circuit consisting of a series of segments denoted by *i* and including entrance and exit losses and an orifice loss,

$$0 = \sum_j \left(\begin{array}{l} g\cos\theta_j \int_j \rho\,dz + \dfrac{G^2}{2D_{h_j}} \int_j \dfrac{4f}{\rho}\,dz + \\ G^2\left(\dfrac{1}{\rho_{out-j}} - \dfrac{1}{\rho_{in-j}}\right) + \quad \dfrac{G^2}{2}\left(\dfrac{K_{in-j}}{\rho_{in-j}} + \dfrac{K_j}{\rho_{out-j}}\right) \end{array} \right) + K_{orf}\,\frac{G^2}{2\rho} \tag{25}$$

This expression is specialized to the case shown in Figure 22. The first term is the gravity head. Let h_{tc} represent the length from the thermal center of the heated zone to the

top of the duct. For an arbitrary axial heat distribution along the heated section, the pressure head due to the density gradient around the loop is

$$\Delta P_h = -(\rho_c - \rho_h)\, g h_{tc} = -\rho_c \beta g h_{tc} \Delta T \tag{26}$$

where we have used the Boussinesq approximation and ΔT is the temperature rise across the heated section. Now assume an axially symmetric heat flux in the heated zone so that from Figure 22

$$h_{tc} = l_c - l_h/2$$

The second term is the friction pressure drop

$$\Delta P_f = 2\frac{f}{D_h}\left(\frac{l_c - l_h}{\rho_h} + \frac{l_h}{(\rho_c + \rho_h)/2}\right) G^2 \tag{27}$$

where a symmetric heat flux distribution in the heated section is assumed. The Boussinesq approximation applied to the above equation gives

$$\Delta P_f = 2\frac{f}{D_h}\frac{l_c}{\bar{\rho}} G^2 \tag{28}$$

where

$$\frac{1}{\bar{\rho}} = \left(\frac{l_c - l_h}{1 - \beta\Delta T} + \frac{l_h}{1 - \beta\Delta T/2}\right)\frac{1}{\rho_c l_c} \tag{29}$$

An integrated average dependence of f on properties is assumed with

$$f = \frac{C}{\left(\frac{GD_h}{\mu}\right)^n} \tag{30}$$

where μ is viscosity and C and n are constants.

The third term is acceleration pressure drop. With the Boussinesq approximation it becomes

$$\Delta P_{acc} = \frac{1}{\rho_c}\left(\frac{\beta\Delta T}{1 - \beta\Delta T}\right) G^2 \tag{31}$$

Collecting these terms Eq. (25) becomes

$$\rho_c \beta \left(\frac{l_c}{l_h} - \frac{1}{2} \right) h_{tc} \Delta T = \left(2 \frac{f}{D_h} \frac{l_c}{\bar{\rho}} + \frac{1}{\rho_c} \left(\frac{\beta \Delta T}{1 - \beta \Delta T} \right) + \frac{1}{2} \left(\frac{K_i}{\rho_c} + \frac{K_o}{\rho_h} + \frac{K_{orf}}{\rho} \right) \right) G^2 \quad (32)$$

where the subscripts *i* and *o* represent the duct inlet and outlet, respectively.

The above expression for the momentum balance is simplified by retaining only the important phenomena. We calculated the relative magnitudes of friction, acceleration, and entrance and exit losses for representative RCCS geometry and conditions and the values are shown in Table 10. These values are based on the GT-MHR data presented in Table 11 which is taken from [7]. The elevation data was scaled from Figure 4.6-1 of [7]. The losses in Table 10 sum to 133 Pa while the gravity head is calculated as 108 Pa. Strictly, these two terms should be equal. However, in the absence of loss coefficient data from [7] we were forced to adopt the temperature rise and velocity given in [7] calculation of losses. Without the loss coefficient data the total losses and buoyant head in Table 10 cannot be expected to be entirely self consistent. The acceleration, exit and entrance losses in Table 10 represent 18 percent of the total losses shown. To the first order then the loop momentum equation can be simplified by dropping all but the friction term yielding

$$\beta g \left(\frac{l_c}{l_h} - \frac{1}{2} \right) \Delta T = 2 \left(\frac{f \, l_c}{D_h} + K \right) \frac{G^2}{\bar{\rho} \, \rho_c} \quad (33)$$

where we have included a generic loss term. This term provides an additional degree of freedom for achieving similarity in an experiment.

We proceed in accord with the notion that when two dissimilar systems satisfy the same set of equations, either system can be used to model the other. [5] We cast both plant and experiment as the same set of equations by nondimensionalizing both plant and experiment equations. Define the dimensionless ratios

$$\theta = \frac{T}{\Delta T_r} \qquad \text{and} \qquad U = \frac{u}{u_r} \quad (34)$$

where ΔTr is the heated section temperature rise at the condition of interest, l_h is the heated section length, and u_r is the heated section inlet velocity at the condition of interest these terms in the denominator are referred to as scaling variables. Expressions for ΔT_r and u_r are obtained from the simultaneous solution of the momentum and energy equations, respectively

$$\beta g \left(\frac{l_c}{l_h} - \frac{1}{2} \right) \Delta T_r = 2 \left(\frac{f \, l_c}{D_h} + K \right) \frac{\rho_c u_r^{\,2}}{\bar{\rho}} \quad (35)$$

$$Q = \rho_c A_h \, u_r \, C_p \, \Delta T_r \quad (36)$$

where A_h is the cross-sectional area of the heated section and Q is the power of the heated section. Then

$$u_r = \left(\frac{\beta g \left(\frac{l_c}{l_h} - \frac{1}{2} \right) \bar{\rho} Q}{\rho_c{}^2 A_h C_p 2 \left(\frac{f l_c}{D_h} + K \right)} \right)^{1/3} \tag{37a}$$

$$\Delta T_r = \frac{Q}{\rho_c A_h C_p u_r} \tag{37b}$$

The momentum equation, Eq. (33), is non-dimensionalized,

$$\left[\frac{g\beta \left(\frac{l_c}{l_h} - \frac{1}{2} \right) \Delta T_r}{u_r{}^2} \right] (\theta_h - \theta_c) = \left[2 \left(\frac{f l_c}{D_h} + K \right) \frac{\rho_c}{\bar{\rho}} \right] U^2 \tag{38}$$

where we have used $\Delta T = T_h - T_c$. The above expression contains two dimensionless groups

$$R = \frac{g\beta \left(\frac{l_c}{l_h} - \frac{1}{2} \right) \Delta T_r}{u_r{}^2} \qquad \text{and} \qquad F = 2 \left(\frac{f l_c}{D_h} + K \right) \frac{\rho_c}{\bar{\rho}} \tag{39}$$

Note that Ri = R/F, the Richardson number.

A.2 Fluid-Energy Conservation

The one-dimensional fluid-energy balance for the air in the heated section in steady state is non-dimensionalized. We have

$$\rho C_p \, u \frac{dT}{dz} = \frac{4h}{D_h} (T_s - T) \tag{40}$$

where u is the fluid velocity, h is the heat transfer coefficient, D_h is the hydraulic diameter defined in Eq. (25) , and T_s is the duct temperature

Non-dimensionalizing the above equation we obtain

$$\frac{1}{\Delta T_r \, l_h} \frac{dT}{d\left(\frac{z}{l_h}\right)} = \frac{4\,h}{\rho\, C_p\, u\, D_h} \left(\frac{(T_s - T)}{\Delta T_r} \right) \quad . \tag{41}$$

Defining the dimensionless ratios

$$Z = \frac{z}{l_h}, \qquad St = \frac{4\,h\,l_h}{\rho\, C_p\, u\, D_h} \left(= 4\,Nu/Re\,Pr \right) \tag{42}$$

gives

$$\frac{d\theta}{dZ} = St\,(\theta_s - \theta) \tag{43}$$

A.3 Similarity Conditions

We seek for the reactor air duct interior the conditions that maintain similitude with respect to loop momentum and heated section fluid energy balances. Now if two dissimilar systems satisfy the same set of equations, then either system can be used to model the other.

The momentum equation for the plant is from Eq. (38)

$$Ri_p\,(\theta_h - \theta_c)_p = U_p^{\,2} \tag{44}$$

and similarly for the experiment

$$Ri_e\,(\theta_h - \theta_c)_e = U_e^{\,2} \tag{45}$$

where the subscript *p* and *e* denote plant and experiment, respectively. If the plant and experiment are to satisfy the same equation then from Eq. (44) and (45) we must have

$$Ri_R = \frac{Ri_e}{Ri_p} = 1 \tag{46}$$

where the subscript *R* denotes the ratio of the experiment to plant. This is the similarity condition. If we are to use the experiment to infer plant behavior we must choose the experiment conditions such that Eq. (46) is satisfied.

The fluid energy equation for the plant is from Eq. (43)

$$\frac{d\theta_p}{dZ_p} = St_p\,(\theta_{s\text{-}p} - \theta_p) \tag{47}$$

and similarly for the experiment

$$\frac{d\theta_e}{dZ_e} = St_e\,(\theta_{s\text{-}e} - \theta_e)\,. \tag{48}$$

If the experiment and plant are to satisfy the same equation then from Eq. (47) and (48) we must have

$$St_R = \frac{St_e}{St_p} = 1 \tag{49}$$

The following two relations among ratios of dimensional variables for achieving similitude are then implied by Eqs. (38), after substitution of Eq. (34), and (49)

$$\left[\left(\frac{l_c}{l_h} - \frac{1}{2}\right)\frac{\bar{\rho}}{\rho_c}\right]_R (\Delta T)_R - \left[\left(\frac{f\,l_c}{D_h} + K\right)\right]_R u_R{}^2 = 0 \tag{50}$$

$$h_R\, l_{hR} - (\rho C_p)_R\, u_R\, D_{hR} = 0 \tag{51}$$

Since we have two equations, similitude between experiment and plant is assured if there are at least two variables that can be set independently in the experiment

B. Multi-Dimensional Effects

Convection heat transfer and pressure loss in the duct interior will likely exhibit some of the same multidimensional phenomena that are present under similar conditions in simpler channel geometries. Such cases can provide useful insight into the phenomena to be expected. In general note that the air duct interior is rectangular is shape, has non-uniform heating of all four walls, has coolant buoyant forces developed internally at the wall, and has a net gravity head that provides a 1-D pressure differential that drives flow. With respect to heating of all four walls and the 1-D pressure differential driving flow, the duct has elements of mixed convection in a vertical heated tube. With respect to rectangular geometry and internal buoyancy phenomena, the duct has elements of buoyancy induced recirculation found between two parallel vertical plates at different temperatures.

B.1 Internal Buoyancy

Heat transfer and pressure loss are a function of the velocity profile in the channel which in turn depends on coolant buoyancy at the wall. Similar to what has been observed experimentally in a heated tube, buoyant forces induced in the fluid nearest the wall by heating of the wall increase the fluid velocity near the wall over the case of no heating. Mass conservation implies that the velocity near the centerline decreases for a net flattening of the velocity profile. This is referred to as aiding flow. The opposite, cooling of the wall, gives rise to opposing flow. Both are shown schematically in Figure 23 [8]. If the flow is turbulent in the non-heated case, arguments based on Prandtl's mixing model suggest that heat transfer is reduced by heating. The effect on heat transfer coefficient is shown in Figure 24 [8]. If the flow in the unheated case is laminar, then heating gives the opposite effect. [9] The heat transfer and pressure loss are known to depend on the following parameters

$$h, f = \Psi\left(\rho, \mu, D_h, u, C_p, k, L, g\beta, \Delta T\right) \tag{52}$$

where D_h is the hydraulic diameter, L is the distance from the entrance, and ΔT is the temperature difference between a wall and the bulk fluid.

The analytic solution for coolant temperature and velocity for laminar natural convection flow between two vertical parallel plates at uniform but different temperatures depends on the same parameters in Eq. (52) [6]. D_h is taken as the distance between the plates and L is the point at which the solution is sought. Although the solution is for the velocity and temperature field between the plates and not the integrated 1-D heat transfer coefficient and friction factor, one notes that the same phenomena can occur inside the air duct and so their parametric dependence as shown by Eq. (52) has applicability to the air duct.

The Pi Theorem applied to both the circular tube and the parallel plate cases as given by Eq. (52) yields

$$Nu = \Psi_{Nu}\left(Re, Gr, Pr, L/D_h\right) \tag{53}$$

$$f = \Psi_{f}\left(Re, Gr, Pr, L/D_h\right) \tag{54}$$

where

$$Nu = \frac{h D_h}{k}, \quad Re = \frac{\rho u D_h}{\mu}, \quad Gr = \frac{g\beta(\Delta T) L^3 \rho^2}{\mu^2}, \text{ and } \quad P_r = \frac{C_p \mu}{k}. \tag{55}$$

Since the air duct interior exhibits elements of the same basic phenomena as the heated vertical circular tube and the vertical parallel plates described above, heat transfer and pressure loss in the air duct interior should depend on these same dimensionless parameters.

The convection regime map for heated vertical circular tubes may have qualitative applicability to the air duct interior. The map, shown in Figure 25, expresses the convection regime in terms of the dimensionless groups in Eq. (55). Demarcation between the mixed and forced convection regime is in terms of these dimensionless numbers.

B.2 Non-Uniform Heat Flux

A dimensional analysis is used to derive similarity relations for a rectangular vertical duct with non-uniform circumferential wall heating. This case differs from the circular tube and parallel plate cases above in that there are four faces and each face has a different uniform temperature, as modeled in Section VI. As a result the more general set of parameters ΔT_{FD}, ΔT_{SD}, and ΔT_{BD} take the place of ΔT in Eq. (52) and the new geometric parameters l_w/ l_d, and l_w are introduced. Radiation heat transport between interior faces is neglected so that all energy leaving an interior face is convected into the duct air stream. From the definition of hydraulic diameter, $D_h = 4A/P_w$, where A is the cross sectional flow area and P_w is the wetted perimeter we have

$$l_w = \frac{1}{2}\left(\frac{l_w}{l_d} + 1\right) D_h . \tag{56}$$

The heat transfer coefficient for face i is then given by

$$h_i = \Omega_i \left(l_w / l_d, \rho, \mu, D_h, u, C_p, k, L, g\beta, \Delta T_i\right), \quad i = \text{FD, SD, or BD.} \tag{57}$$

Define an average temperature and an average heat flux

$$\overline{\Delta T} = \frac{l_w \Delta T_{FD} + 2 l_d \Delta T_{SD} + l_w \Delta T_{BD}}{2\left(l_w + l_d\right)} \tag{58}$$

and

$$\overline{\Delta q''} = \frac{h_{FD} l_w \Delta T_{FD} + 2 h_{SD} l_d \Delta T_{SD} + h_{BD} l_w \Delta T_{BD}}{2\left(l_w + l_d\right)} . \tag{59}$$

Define an average circumferential heat transfer coefficient as the ratio of Eq. (59) to Eq. (58) and substitute Eq. (57) into Eq. (59) to obtain

$$\overline{h} = \frac{\overline{q''}}{\overline{\Delta T}} = \Omega\left(l_w / l_d, \rho, \mu, D_h, u, C_p, k, L, g\beta, \Delta T_{FD}, \Delta T_{SD}, \Delta T_{BD}\right) \tag{60}$$

where we have used Eq. (56) to express l_w in terms of l_w/l_d and D_h . Now from Eq. (58), ΔT_{SD} in the above equation can be expressed in terms of the average temperature and ΔT_{FD} and ΔT_{BD} so that

$$\bar{h} = \Omega \left(l_w / l_d, \rho, \mu, D_h, u, C_p, k, L, g\beta, \Delta T_{FD}, \Delta \bar{T}, \Delta T_{BD} \right) \tag{61}$$

Eq. (61) is non-dimensionalized using the Pi Theorem. Choose the fundamental dimensions M (mass), L (length), θ (time), T (temperature), and H (energy) and primary quantities ρ, L, μ, ΔT, and k. Solving for the Π terms gives

$$\overline{Nu} = \Psi (Re, \overline{Gr}, Pr, L/D_h, l_w/l_d, \Delta T_{FD}/\Delta \bar{T}, \Delta T_{BD}/\Delta \bar{T}) \tag{62}$$

where the term on the left is the Nusselt number based on the average circumferential heat transfer coefficient. The last two terms on the right side are re-written using Eq. (60) and the definition of the heat transfer coefficient for a wall as

$$\frac{\Delta T_i}{\Delta \bar{T}} = \frac{q_i''}{\bar{q}''} \frac{\bar{h}}{h_i} \quad , i = \text{FD or BD.} \tag{63}$$

But from Eq. (60) and (57) the two heat transfer coefficients in the above equation are functions of parameters already introduced so that Eq. (62) can alternatively be written as

$$\overline{Nu} = \Psi (Re, \overline{Gr}, Pr, L/D_h, l_w/l_d, q''_{FD}/\bar{q}'', q''_{BD}/\bar{q}'') \tag{64}$$

That is, this average Nusselt number for the rectangular duct with non-uniform circumferential heat flux is dependent on the same dimensionless numbers as the circular tube case plus three additional parameters, the duct aspect ratio and the fractional heat flux into the duct front and back faces.

The friction factor is derived similarly and therefore has the same dependence as Eq. (64).

B.3 Similarity Conditions

We seek for the air duct interior the conditions that maintain similitude with respect to heat transfer and pressure loss phenomena in a vertical channel with internal buoyancy with circumferentially non-uniform wall heating and a rectangular cross sectional shape. Now if two dissimilar systems satisfy the same set of equations, then either system can be used to model the other. Thus, given the functional dependence of the Nusselt number on the dimensionless groups appearing in Eq. (64), if the experiment meets the conditions

$$\mathrm{Re}_R = 1, \quad \overline{\mathrm{Gr}}_R = 1, \quad \mathrm{Pr}_R = 1, \quad (L/D_h)_R = 1,$$
$$(l_w/l_d)_R = 1, \quad (q''_{FD}/\overline{q}'')_R = 1, \quad (q''_{BD}/\overline{q}'')_R = 1 \tag{65}$$

where the subscript *R* denotes the ratio of the experiment to plant, then we have for the heat transfer coefficient

$$\overline{h}_R = \frac{k_R}{D_{hR}}. \tag{66}$$

That is, the heat transfer coefficient in the plant is obtained from the value in the experiment according to Eq. (66) with the required similarity conditions given by Eq. (65).

Note that this average circumferential heat transfer coefficient is appropriate for use in one-dimensional fluid-energy models as in Eq. (40). In fact, we specifically derived it for such use.

VII. REVIEW OF EXISTING NSTF DATA

The NSTF was built in the 1980s to provide data for use in developing and refining models for predicting the performance of natural convection air cooling systems in liquid metal reactors. The geometry and the conditions in the heated test section of NSTF qualitatively resemble those of the air duct in the RCCS. The test section is rectangular in cross section with a heated face and a reflective opposite face. Air is drawn in at the inlet, is heated, expands, and rises exiting the NSTF through the chimney mounted above the test section. The main dimensions appear in Figure 26.

A series of tests involving both finned and bare surfaces in the rectangular heated test section were performed. The current RCCS air design does not employ fins in the interior of the air duct and so we review only the NSTF experiments that did not involve finned heat transfer surfaces. There were 71 such tests, the records of which have been preserved in the NSTF database. A review of those materials shows that some of the issues addressed in the NSTF experiments are the same issues of interest in RCCS performance. These include the effect of buoyancy on velocity profile in vertical heated channels and its impact on pressure drop and heat transfer.

The NSTF database consists of a master electronic index of the records from the experiments performed in the Natural Shutdown Test Facility (NSTF) in the 1980s and the records themselves. The records consist of reports, memos, experiment data printouts, magnetic tapes, blueprints, and design data that were archived at the time of the facility shutdown. Each record is labeled with a unique number that appears along with a description of the record in an Access database. A typical entry lists the type of data, the author, a title, the date, and comments about the record. The Access database provides a

convenient means for searching for documents and identifying their location as the need arises.

The applicability of the NSTF data to the development of heat transfer and pressure loss models in forced, mixed, and natural convection regimes for the RCCS air duct was investigated. The basic premise is that if for the important governing equations the corresponding dimensionless numbers are preserved between plant and experiment, then data from one can be used to describe the other. The relevant equation is Eq. (64) and the relevant dimensionless numbers appear on the right-hand side. We were able to readily calculate the first five dimensionless numbers. Table 12 summarizes the values of the dimensionless numbers from data archived from experiments completed in the NSTF. The table contains a representative subset of experiments that span the conditions of all 71 unfinned experiments. The Grashof number $Gr_{\delta T}$ is calculated according to Eq. (55) and is shown in the second column from the right. In the first column on the right the Grashof number $G_{rq"}$ assumes the heat flux is related to the temperature difference between the wall and bulk fluid by $q" = k/D_h\ \delta T$. This is obviously an approximation but is useful when direct measurement of the temperature difference is not available. In the case of the NSTF both q" and δT are available from the experiment and given in Table 12. Note the ratio of $Gr_{\delta T}$ to $G_{rq"}$ is about 1/200. Similarly, for the RCCS we computed dimensionless numbers for the air duct interior. The conditions in the RCCS at full power are given in Table 13. During cooldown accidents the peak conditions are not much greater than those in Table 13. Tables 14 and 15 give the Reynolds and Grashof numbers, respectively. The Grashof number presented in Table 15 is $G_{rq"}$ and is computed from the heat flux as shown in Table 15. Figure 27 shows the data in these tables plotted along side each other. Also shown is our estimate for $Gr_{\delta T}$ for the RCCS. This was obtained from the value for $G_{rq"}$ for the RCCS by scaling by the factor 1/200 described above that relates $Gr_{\delta T}$ to $G_{rq"}$ for the NSTF. It is assumed that the quality of the approximation $q" = k/D_h\ \delta T$ is the same for the RCCS and the NSTF.

Several comments and observations are made for the data in Figure 27. The figure shows the demarcations between forced, mixed, and natural convection as given by [9]. Based on these lines, it appears from the data plotted with respect to $Gr_{\delta T}$ that NSTF data exist for both the mixed convection and natural convection regions. In addition, the estimated RCCS operating point appears to be in the middle of the mixed convection region. While the data show exact scaling of Re and Gr is not achieved for convection in the duct interior between the NSTF and the RCCS, the mixed convection region where the RCCS air duct is expected to operate is preserved. The NSTF data offer an opportunity to validate CFD codes in the mixed convection region for Reynolds numbers between 37,700 and 170,000 and Grashof numbers between $8x10^8$ and $3.5x10^9$. Some extrapolation would be required to analyze the RCCS air duct at a Reynolds number of 14,000 and Grashof number of 10^7 where it is expected to operate. However, since the convection mode remains the same, if a single set of turbulence parameters give consistent predictive behavior over the range of NSTF data, we might have confidence in extrapolating down to RCCS conditions.

IX. SCALABILITY OF FUTURE VHTR NSTF EXPERIMENTS

One objective of a scaling analysis is to study the effect on similitude of distortions in geometry introduced in an NSTF experiment. Let us assume the experiment is to be full scale. This condition will be met by the duct cross section and by the gap between ducts since the plan is to fabricate them as such. It will not be met in the experiment, however, by 1) the length of the heated section (11m rather than 17 m), 2) the distance between the vessel surface and the front duct face (0.1 m instead of 0.7 m), and 3) the number of ducts (twelve versus tens). We describe using the similitude conditions derived in Sections VI and VII how the experiments can be run to compensate for these geometry distortions.

A. Air Duct: Heated Length

The height of the test chamber in the NSTF limits the length of the heated section to less than in the plant. Nonetheless, it was shown that similitude with respect to integral one-dimensional behavior can be achieved if the Richardson and Stanton numbers are preserved. The conditions for doing so are given by Eqs. (50) and (51). There are two degrees of freedom available to do so, the loss coefficient and the heated section power. Thus, a separate effects experiment can be performed to generate data for plant integral behavior.

B. Air Duct: Vessel-to-Duct Spacing

The width of the test chamber in the NSTF limits the distance between the plate that simulates the reactor vessel and the front face of the duct. A concern is that failure to match this dimension will alter the split of energy flow among the duct faces and result in non-similitude with respect to the heat transfer and friction factor processes inside the air duct. A first step then is to determine the conditions needed to maintain similitude with respect to these phenomena. Eq. (65) gives the conditions required and includes the condition that the ratios of energy fluxes between duct faces be preserved. The feasibility of achieving this latter condition is addressed next.

C. Reactor Cavity: Vessel-to-Duct Spacing

It is important as described above to preserve between the plant and the experiment the energy flow split among the duct faces. The main issue is the effect of the distance between the vessel and the front face of the ducts on the vessel-to-duct view factors. It turns out that these view factors are independent of this distance. This was demonstrated both computationally for representative duct dimensions using the expressions for view factors given by Eqs. (6a) and (6b) and in a simple thought experiment. The representative duct dimensions and corresponding view factor values are given in Table 16. As for the thought experiment, consider the case where the vessel and back wall have been brought into contact with the front and back faces of the ducts, respectively. Two adjacent ducts then define a rectangular enclosure bordered by two duct sides and the vessel and back walls. Now the side-wall-to-vessel view factor is equal

to unity minus the side-wall-to-side-wall view factor and the side-wall-to-back-wall view factor. Now if the vessel is moved away from the duct the values of these last two view factors do not change. Hence, the side-wall-to-vessel view factor is not altered. By reciprocity, the vessel to side-wall view factor is also unchanged.

It was shown that preserving the view factors will ensure that the energy flow split referred to above is preserved. In turn, as just shown, these view factors are independent of the distance between the vessel and the front face of the ducts. Thus, the heat transfer and friction factor processes inside the duct are independent of the vessel to duct distance.

D. Edge Effects

There is no net heat flow across the line of symmetry between adjacent ducts in the actual plant geometry. However, in the NSTF experiment there will be a heat loss component in the test section through the outboard side wall of the end duct. There is therefore a need to minimize the influence of end walls in the NSTF experiment. This can be achieved by moving the heaters close to the front face of the ducts to achieve a high aspect ratio between the width of heater and the distance from heaters to duct as shown in Figure 28. To the extent the heater width is very large compared to the width of a unit cell (duct plus gap) the view factors of the duct faces with respect to the heater for all but the last few ducts on the end are unchanged.

IX. CONCLUSIONS

Passive safety in the Very High Temperature Reactor (VHTR) is strongly dependent on the thermal performance of the Reactor Cavity Cooling System (RCCS). Scaled experiments performed in the Natural Shutdown Test Facility (NSTF) are to provide data for assessing and/or improving computer code models for RCCS phenomena with the goal of achieving a high degree of certainty in predicted design heat removal rate. The computer code models are to be used in design studies and safety analyses that will support licensing of the VHTR. To guide in the selection and development of an appropriate set of experiments a scaling analysis has been performed for the air-cooled RCCS. The goals were to 1) determine the phenomena that dominate the behavior of the RCCS, 2) determine the general conditions that must be met so that these phenomena and their relative importance are preserved in the experiments, 3) identify constraints specific to the NSTF that potentially might prevent exact similitude, and 4) then to indicate how the experiments can be scaled to prevent distortions in the phenomena of interest.

The phenomena identified as important to RCCS operation were also the subject of a recent PIRT study. That work and the present work collectively indicate that the main phenomena influencing RCCS heat removal capability are 1) radiation heat transport from the vessel to the air ducts, 2) the integral effects of momentum and heat transfer in the air duct, 3) buoyancy at the wall inside the air duct giving rise to mixed convection, and 4) multidimensional effects inside the air duct caused by non-uniform circumferential heat flux and non-circular geometry.

Investigations were conducted to quantify the effect of neglecting buoyancy at the wall on heat transfer and pressure drop in the air duct and in turn on key safety parameters. The literature shows that the ratio of friction factor in a heated to unheated pipe for vertical upflow increases in an unbounded manner as the Grashof number increases. A factor of two is easily achievable. Similarly, the ratio of heat transfer coefficients can assume a value as low as 0.5. Simulations with RELAP showed that the vessel wall temperature is more sensitive to changes in air duct friction factor and heat transfer coefficient than peak fuel temperature. A doubling of the friction factor increases vessel temperature by 20C while a halving of the heat transfer coefficient increases vessel temperature by 25C. Thus, similarity experiments aimed at obtaining mixed convection data in the NSTF can contribute to improved predictions of the RCCS heat removal capabilities. One can take advantage of this by reducing safety margins to improve plant economics.

The NSTF provides a capability for full-scale experiments in all but two geometric dimensions. The dimensions are 1) the distance from the vessel surface to the front of the duct face and 2) the length of the heated section. The scaling analysis showed, nevertheless, that similitude can be preserved for the above four phenomena on an individual basis if they are regarded as separate effects. Furthermore, the distribution of heating on the duct faces is not affected by (1). The heat flow into the test section and the air duct loss coefficient provide two independent degrees of freedom and can be used to tailor experiment conditions to achieve similitude in each instance. Additionally, by

introducing further degrees of freedom, such as the duct aspect ratio and the distance between ducts, it may be possible to achieve similitude for more than one of these separate effects simultaneously in a single experiment. This is left as a task for the next phase of the project which is to produce an experiment test plant in conjunction with the refurbishment of the facility. This is in preparation for the performance of VHTR-focused experiments in the NSTF.

Review of the current NSTF database accumulated from past experiments performed for the IFR program indicates that from the scaling perspective, more than half of the 71 unfinned experiments performed are in the mixed convection region, the region where the RCCS air duct is expected to operate. Thus, while the data indicate exact scaling of Reynolds and Grashof numbers between the NSTF and the RCCS is not achieved in the duct interior, the mixed convection phenomenon is preserved. The NSTF data offer an opportunity to validate CFD codes in the mixed convection region for Reynolds numbers between 37,700 and 170,000 and Grashof numbers between $8x10^8$ and $3.5x10^9$. Some extrapolation would be required to analyze the RCCS air duct at a Reynolds number of 14,000 and Grashof number of 10^7 where it is expected to operate. However, since the convection mode remains the same, if a single set of turbulence parameters give consistent predictive behavior over the range of NSTF data, we might have confidence in extrapolating down to RCCS conditions.

X. REFERENCES

1. Jean-Claude Gauthier, Gerd Brinkmann, Bernie Copsey, and Michel Lecomte, "ANTARES: The HTR/VHTR Project at Framatome ANP," Second International Topical Meeting on High Temperature Reactor Technology, Beijing, China, September 22-24, 2004.

2. *450 MWt Reactor Cavity Cooling System System Design Description*, DOE-HTGR-90016, Revision 0, Bechtel National, Inc., November 1993.

3. R.B. Vilim *et al*, "Initial VHTR Accident Scenario Classification: Models and Data," ANL-GenIV-057, September 2005.

4. C. Tzanos, personal communication, Argonne national Laboratory, Febraury 2005.

5. M.P. Heisler, "Development of Scaling Requirements for Natural Convection Liquid-Metal Fast Breeder Reactor Shutdown Heat Removal Test Facilities," Nucl. Sci. Eng. 80, p. 347, 1982.

6. W. M. Rohsenow and H. Choi, "Heat Mass and Momentum Transfer," Prentice Hall, 1961.

7. Gas Turbine-Modular Helium Reactor (GT-MHR) Conceptual Design Report, Report number 910720/1, General Atomics, July 1996.

8. T. Aicher and H. Martin, New Correlations for mixed turbulent natural and forced convection heat transfer in vertical tubes," International Journal of Heat and Mass Transfer, Vol. 40, No.15, pp. 3617-3626, 1997.

9. W. Williams, P. Hejzlar, M.J. Driscoll, W.J. Lee, and P. Saha, "Analysis of a Convection Loop for GFR Post-LOCA Decay Heat Removal form a Block-Type Core," MIT-ANL-TR-095, March 2003.

The flow through the reactor core (fuel) and reflectors is vertically downward where it exits into a common outlet plenum that is in line with the hot duct shown on the lower left. The flow exits the vessel through the hot duct where it is transported to the power conversion unit (PCU). The reactor coolant inlet duct is an annulus that is concentrically located around the hot duct. The inlet flow, which comes from the PCU, enters a plenum below the outlet plenum where it is transported through vertical ducts, located between the core barrel and the reactor vessel, to a plenum in the upper part of the reactor vessel. The reactor core is annular and is surrounded by reflectors on the top, bottom, and both annular sides. In the figure the core is the red region inside the dashed rectangles. A top cutaway view of the reactor vessel shows there are three concentric rings of hexagonal fuel assemblies surrounding an inner reflector of hexagonal assemblies and surrounded by an outer reflector largely made of hexagonal assemblies. The core barrel is along the perimeter of the outer reflector. The reactor fuel is inside rods that are located in vertical holes in the hexagonal graphite core blocks. There are vertical coolant holes in the hexagonal fuel blocks.

There are 102 hexagons representing the entire core regions. Each of these hexagons represents a vertical stack of 10 fuel blocks and an assembly lower reflector below the fuel stack and an assembly upper reflector above it. Similarly, most, if not all of the hexagons that represent inner or outer reflectors, are a slice through a stack of hexagonal graphite blocks.

The reactor is to be located in a concrete silo that is below grade. This silo will be vented so that the walls of the silo will not be subjected to high pressure should a breach in the reactor pressure boundary cause high-pressure helium to enter the reactor cavity, which is the space between the reactor vessel and the inner surfaces of the silo.

Heat given off from the surface of the reactor vessel would cause the silo to heat up considerably if an effective means of heat rejection to the atmosphere were not provided. This means is the reactor cavity cooling system (RCCS). For the proposed RCCS design vertical intake ducts through the top of the silo transport outside air to plena near the bottom of the silo. The air then travels upward through 292 vertical heating panels, or RCCS ducts, and ultimately out through the exhaust ducts above the silo. These 292 ducts are 2 inches by 10 inches in exterior dimensions and are spaced along inside of the rectangular boundary of the reactor cavity on a 4-inch pitch with one of the 2-inch sides facing the reactor vessel. This system is designed so that the outside air used for removing heat is completely separated from the rest of the air inside the silo. The air inside the RCCS ducts is heated by heat transferred, mostly by radiation, from the surface of the reactor vessel. The air flow through the RCCS is driven entirely by natural convection caused by the air in the RCCS ducts being less dense than the cold air entering from outside. The RCCS not only protects the concrete walls of the silo from excessive temperatures, but also provides an essential heat removal system during the PCC and DCC transients under consideration. For these transients, once the compressors

have stopped, the RCCS is part of the only path through which reactor decay heat can be rejected.

In the RELAP5 model of the reactor cooling circuit the helium flow originates in node 100 and travels through the vessel inlet plenum (note 110) and upward through the reactor riser (node 130), located between the reactor vessel and the core barrel. The flow then goes from the riser to the core inlet plenum (node 140). The structure at the top of node 140, which is the reactor vessel upper plenum shield, does not block the flow path, but merely absorbs and conducts heat from the passing flow. There are five parallel paths that connect to the core inlet plenum. The one labeled 142 represents the inner reflector of the reactor. The one labeled 145 represents the outer reflector of the reactor. The solid structure in region 145 models both the outer reflector graphite material and the core barrel. The three paths, 152, 154, and 156, represent the three concentric rings of core hexagonal assemblies.

In the model, each of the three core regions (152, 154, and 156) has 12 axial nodes. The top and bottom nodes represent the upper and lower reflector, respectively. The ten middle nodes represent the stack of ten core blocks. The inner and outer reflector regions each have 12 axial nodes. In the model the nodes in the five regions are aligned to form 12 horizontal layers. Thus, the two reflector and three core regions taken together have a total of 5×12, or 60 nodes. Each of the four inner regions (inner reflector and three core regions) employs the same geometric model to represent its 12 axial nodes, which is a number of identical concentric annuli with coolant going through the center surrounded by a multilayer solid annulus. This solid annulus is used to represent the fuel and graphite of each region. The diameter of the coolant hole in the middle is that of the coolant channels in the reactor. Each annulus represents one coolant hole and the fuel and graphite associated with it. The number of identical annuli in each of these four each regions is specified so that the amount of fuel, graphite, and coolant in each is accurately represented. In the model the solid materials of the outer reflector and the core barrel are combined into two concentric annular layers of the outer reflector region. The geometry of the core barrel is as in the reactor and the amount of graphite in the outer reflector is properly represented. The coolant channel that is attached to this region is represented with the proper hydraulic parameters, such as hydraulic diameter and flow area.

RELAP5/ATHENA permits heat to be transferred from any one of these 60 nodes to any other. This is accomplished by a 60×60 matrix that, in a manner analogous to radiation view factors, allows conduction from any of the 60 solid nodes to any of the other 59. The rate of heat transfer from one solid node to another is specified as a conductance, which is defined as a material conductivity divided by a conduction length. This heat conduction matrix is used to represent heat transfer in the horizontal direction from one reflector or core region to immediately adjacent ones. It is also used to approximate axial heat transfer within each of the five reflector and core regions. This is accomplished by the use of a conduction path that connects the vertical surface of a node to the same vertical surface of the node immediately above or below it.

The radial conductance between adjacent horizontal regions assumed that two solid hexagonal blocks were in perfect contact with each other. The conduction length was taken to be the distance from the center of one hexagon to the center of the other while the two were in contact along a common side. The conductivity used in determining the conductance was taken to be a weighted average of the graphite matrix and fuel cross-sectional areas. No reduction in conductivity was taken for the presence of the coolant hole in the blocks. No gap or contact resistance was included where the two hexagons come together. Therefore, the resultant conductances are expected to be on the optimistically high side.

In the RELAP5/ATHENA representation of the RCCS the downcomer is part of the inlet path for the outside air. Heat that is radiated from the reactor vessel, in addition to heating the RCCS ducts, also heats the downcomer and the concrete wall of the silo. In the model the concrete wall and the earth beyond it are both represented. The source of outside air is node 950 and the sink is node 980. The downcomer is region 960, the common plenum is node 965, and the 292 identical RCCS ducts are represented by region 970. Region 900 represents the air contained inside the reactor cavity that does not flow through the RCCS ducts.

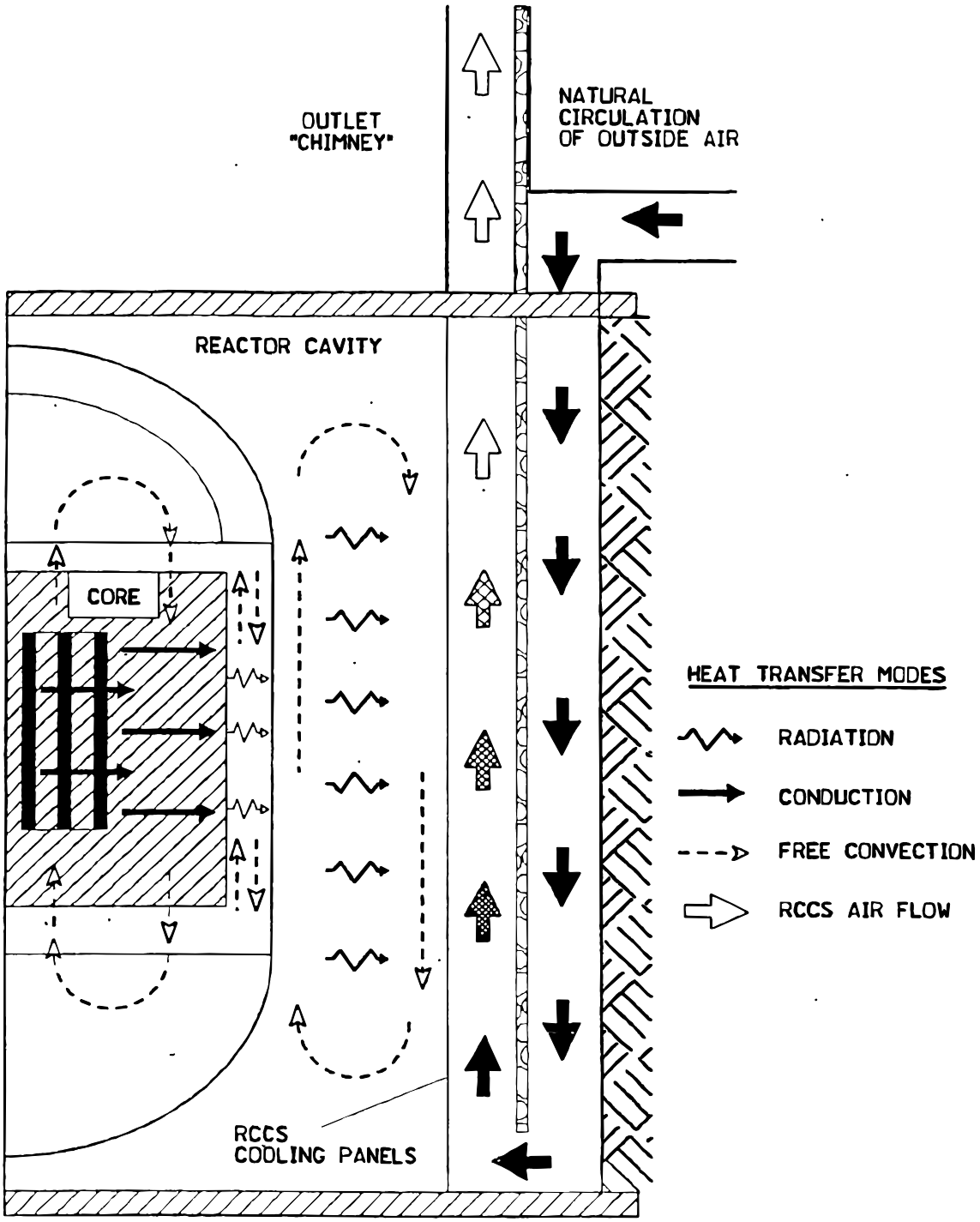

Figure 1. MHTGR Passive Heat Transfer Mechanisms

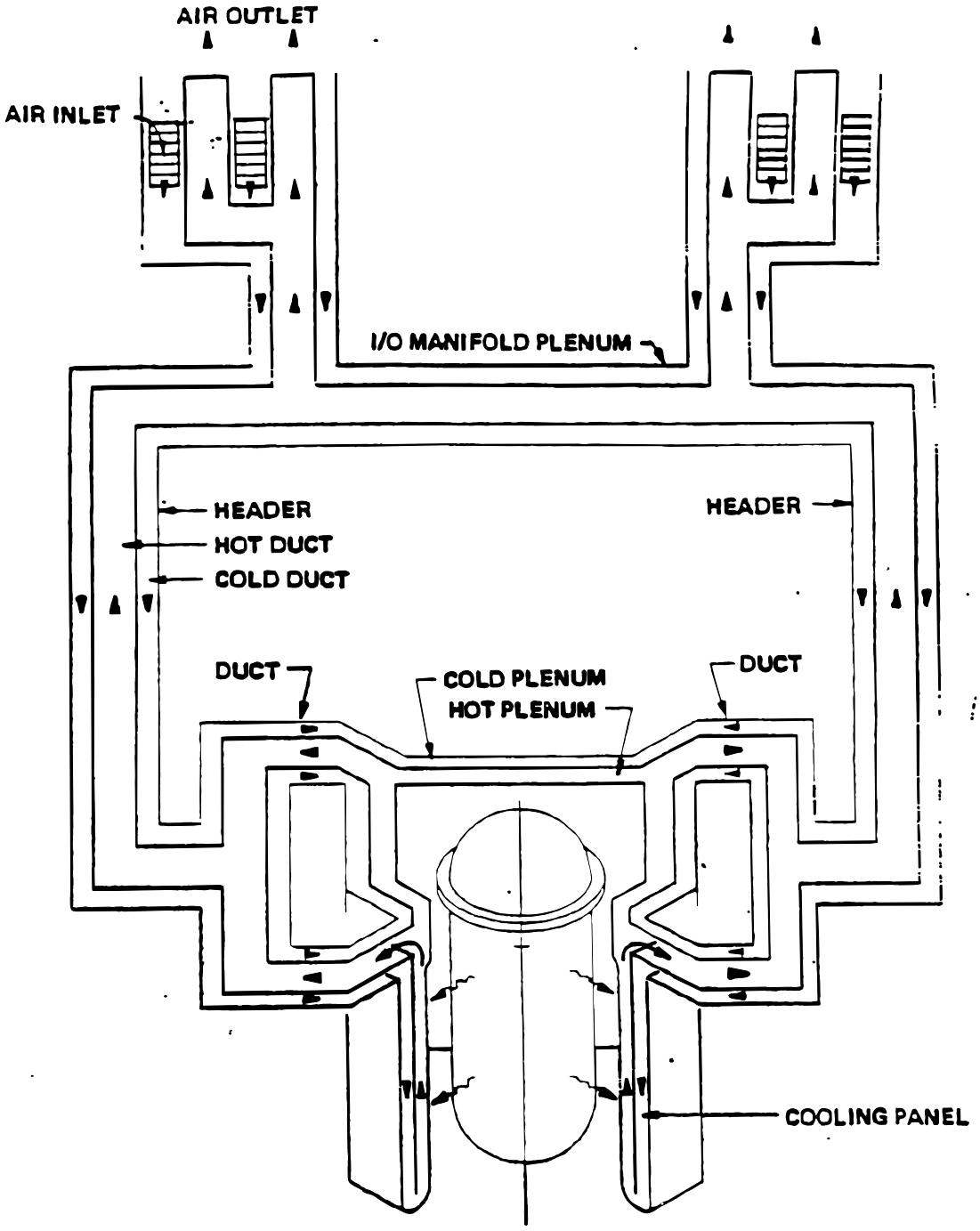

Figure 2. Schematic RCCS Air Flow Configuration

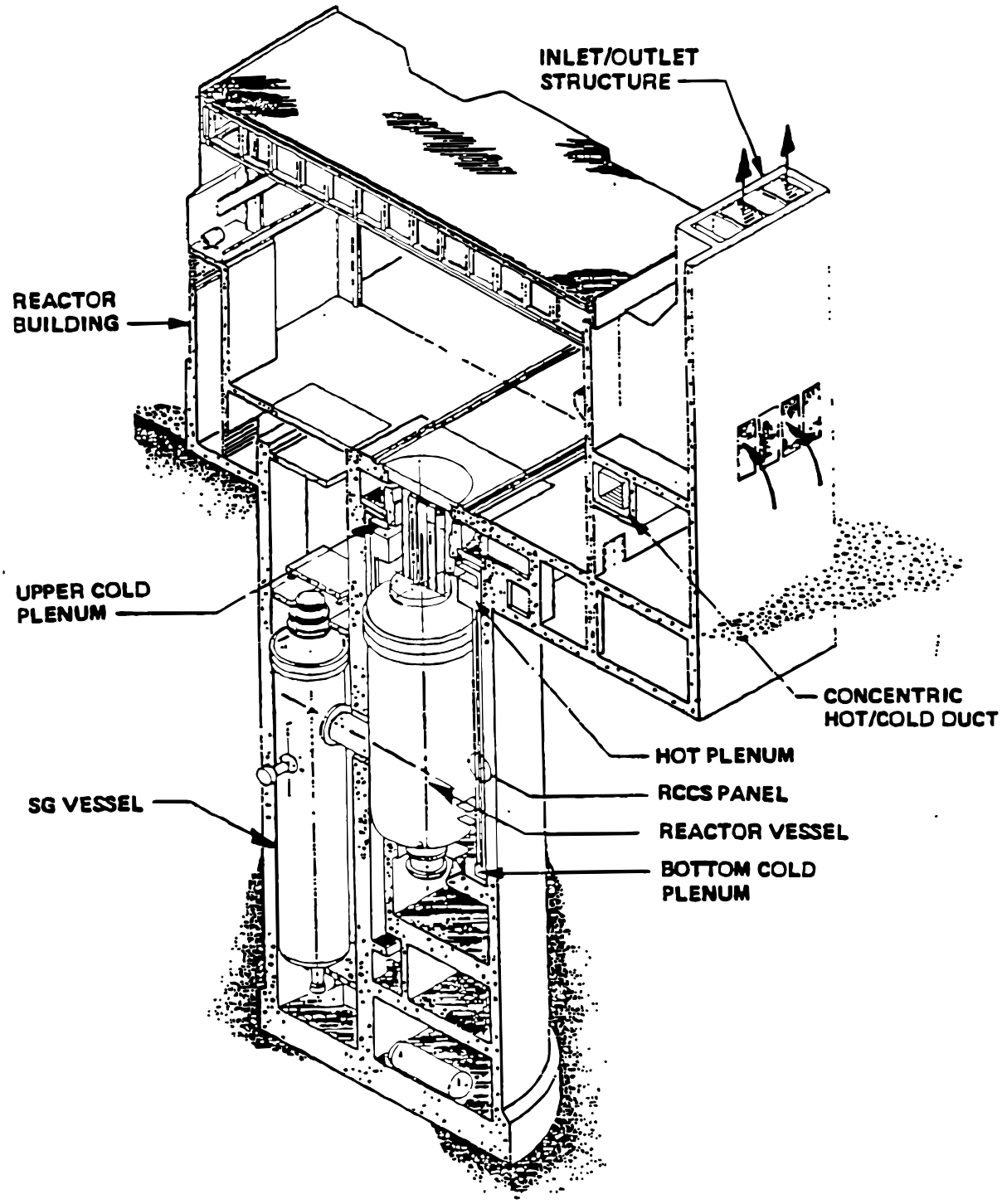

Figure 3. Overall RCCS Configuration

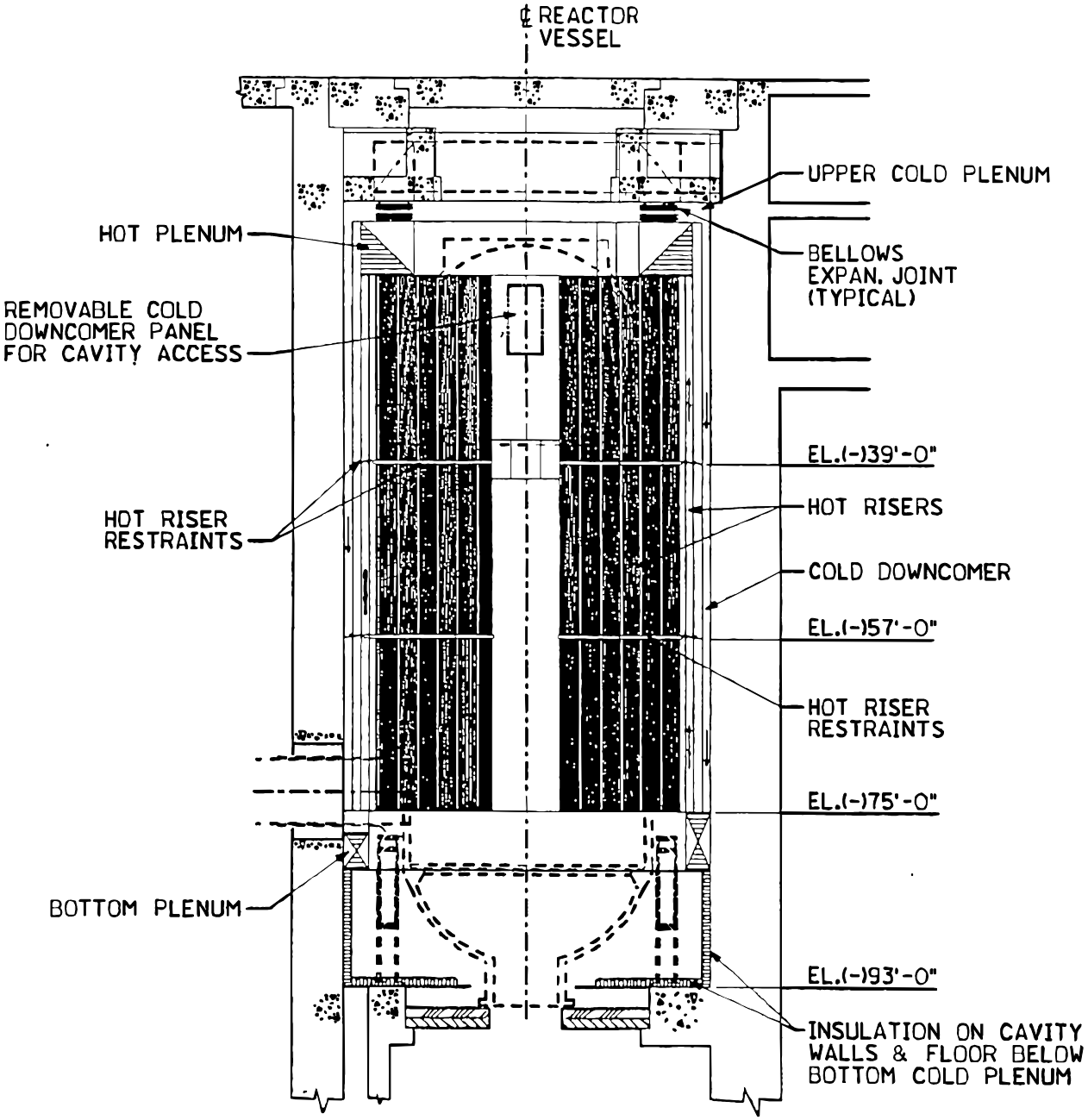

Figure 4. RCCS Panel Configuration – Cross Section

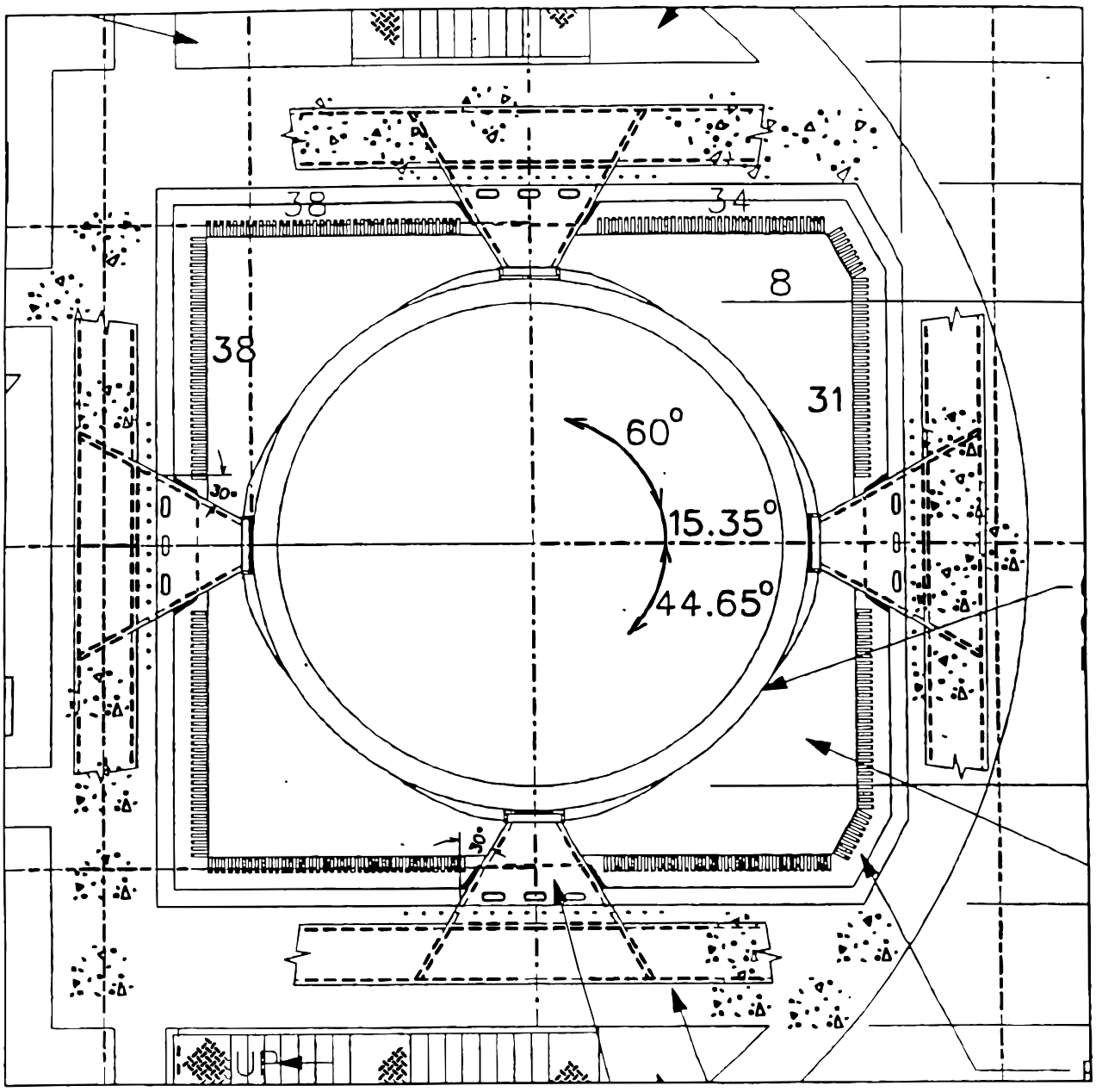

Figure 5. RCCS Panel Configuration – Plan

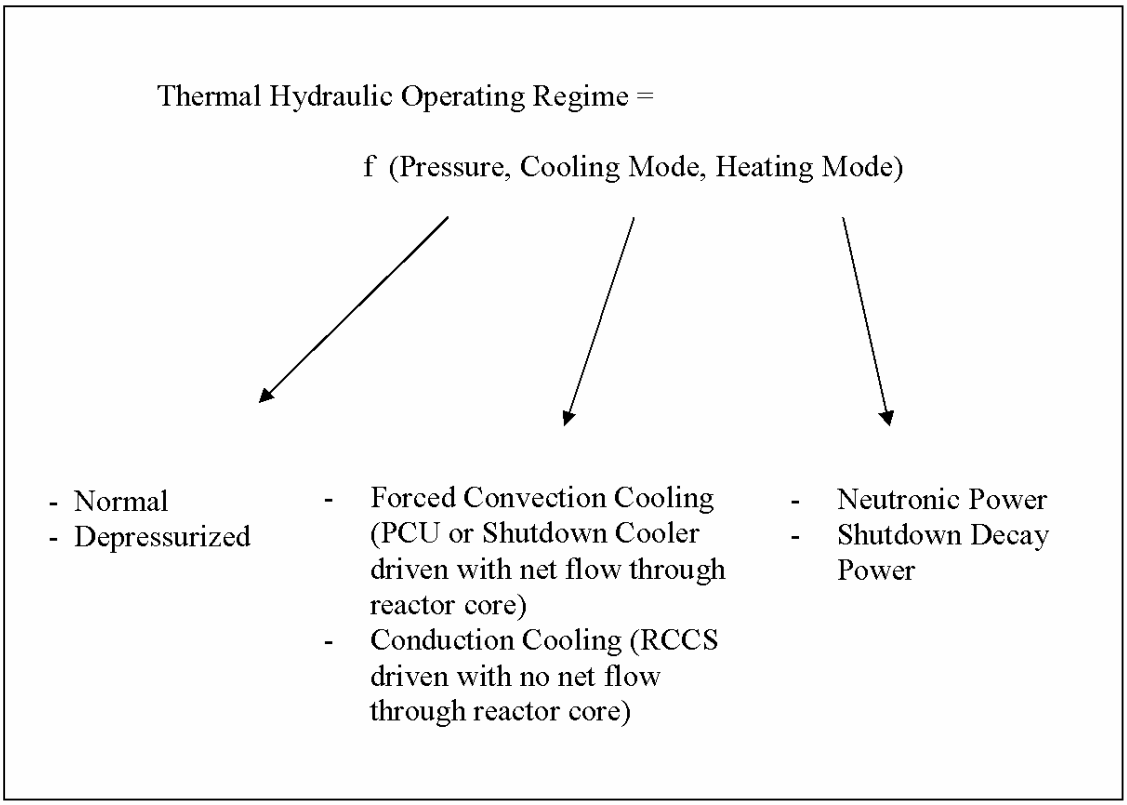

Figure 6 Factors Influencing Thermal-Hydraulic Operating Regime

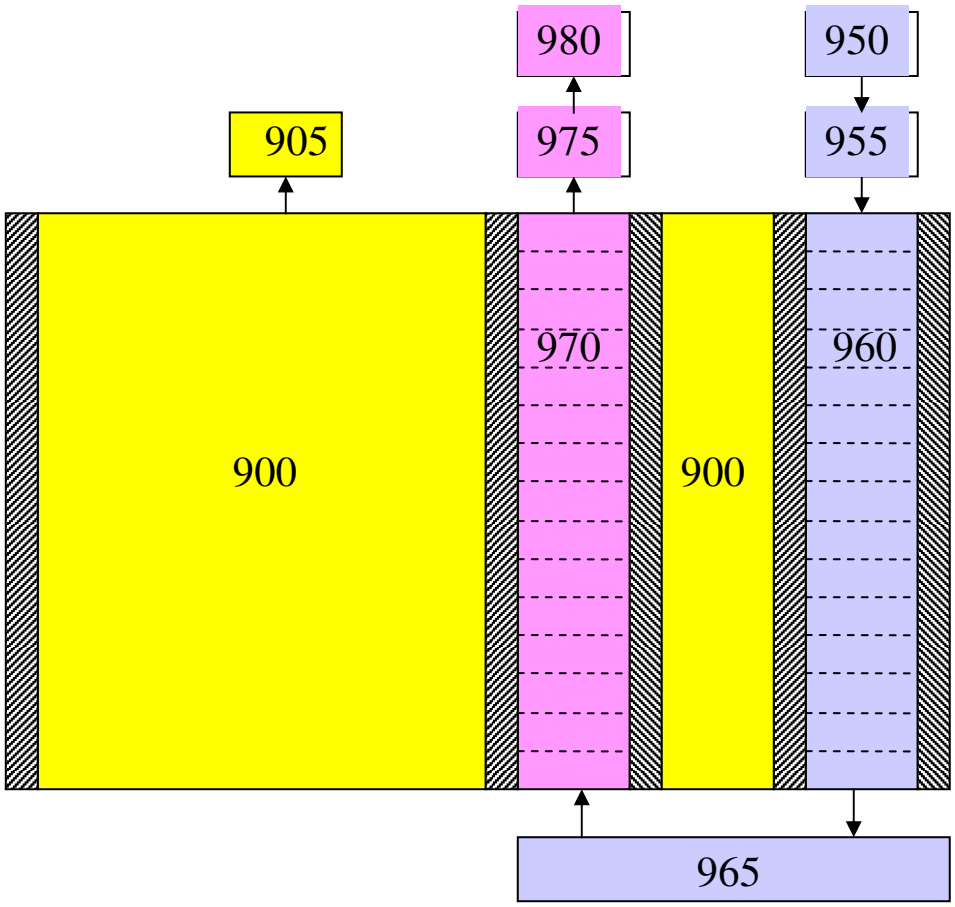

Figure 7. VHTR Reactor Cavity Nodalization

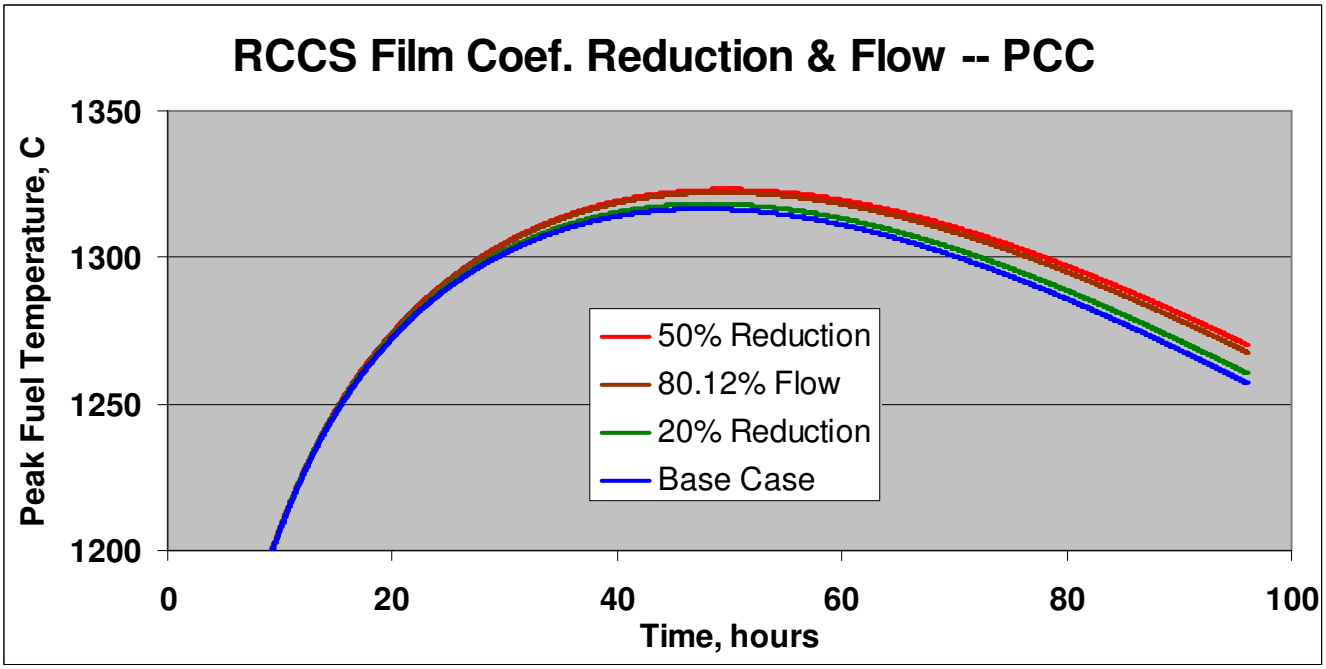

Figure 8. Effect of RCCS Film Coefficient and Initial Air Flow Rate on the Peak Fuel Temperature for the Pressurized Conduction Cooldown

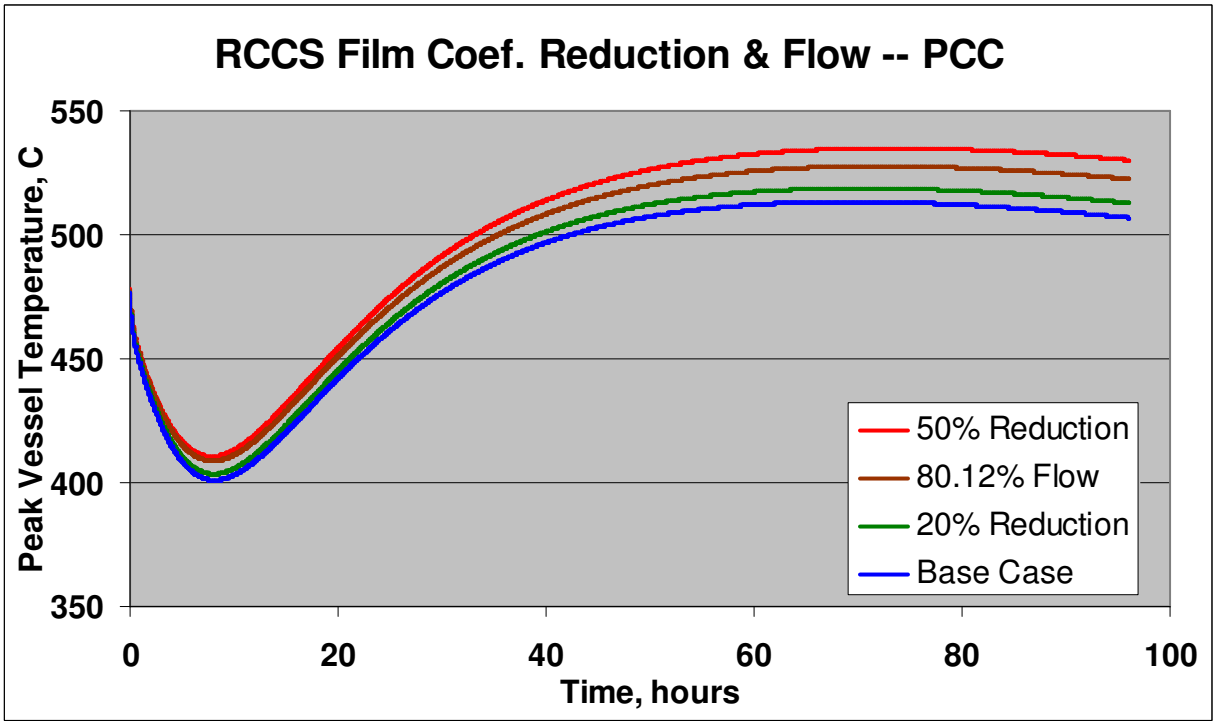

Figure 9. Effect of RCCS Film Coefficient and Initial Air Flow Rate on the Peak Reactor Vessel Temperature for the Pressurized Conduction Cooldown

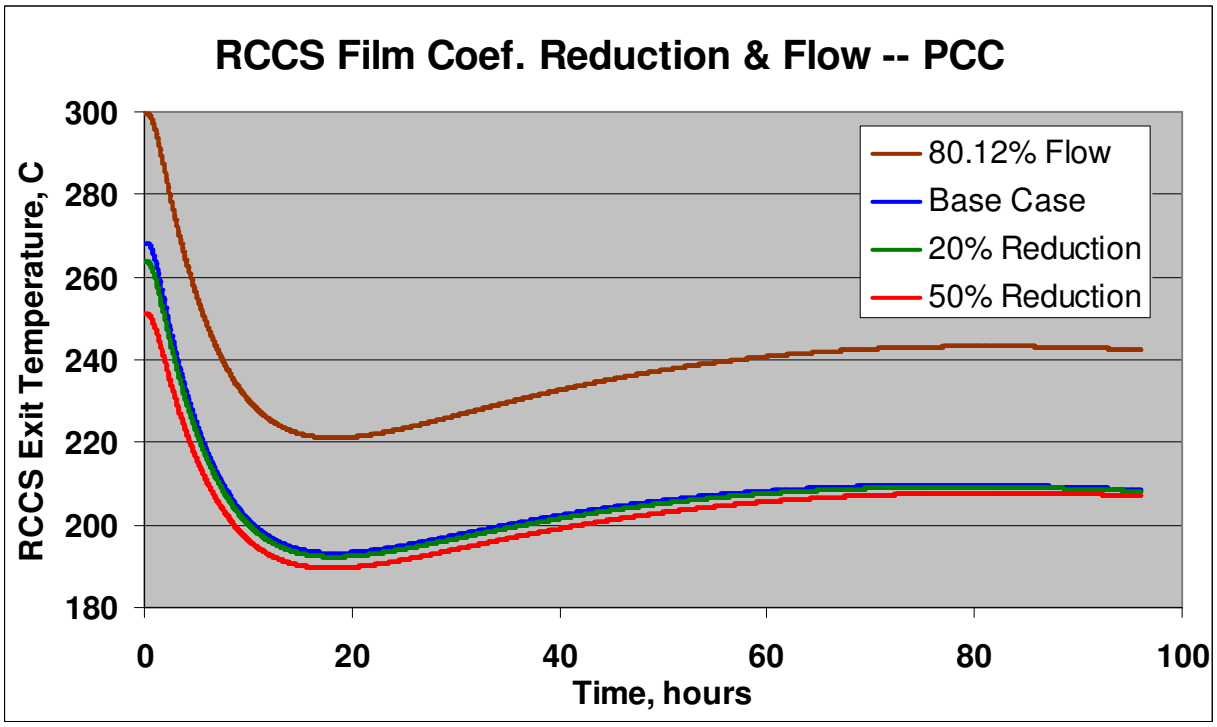

Figure 10. Effect of RCCS Film Coefficient and Initial Air Flow Rate on the RCCS Exit Coolant Temperature for the Pressurized Conduction Cooldown

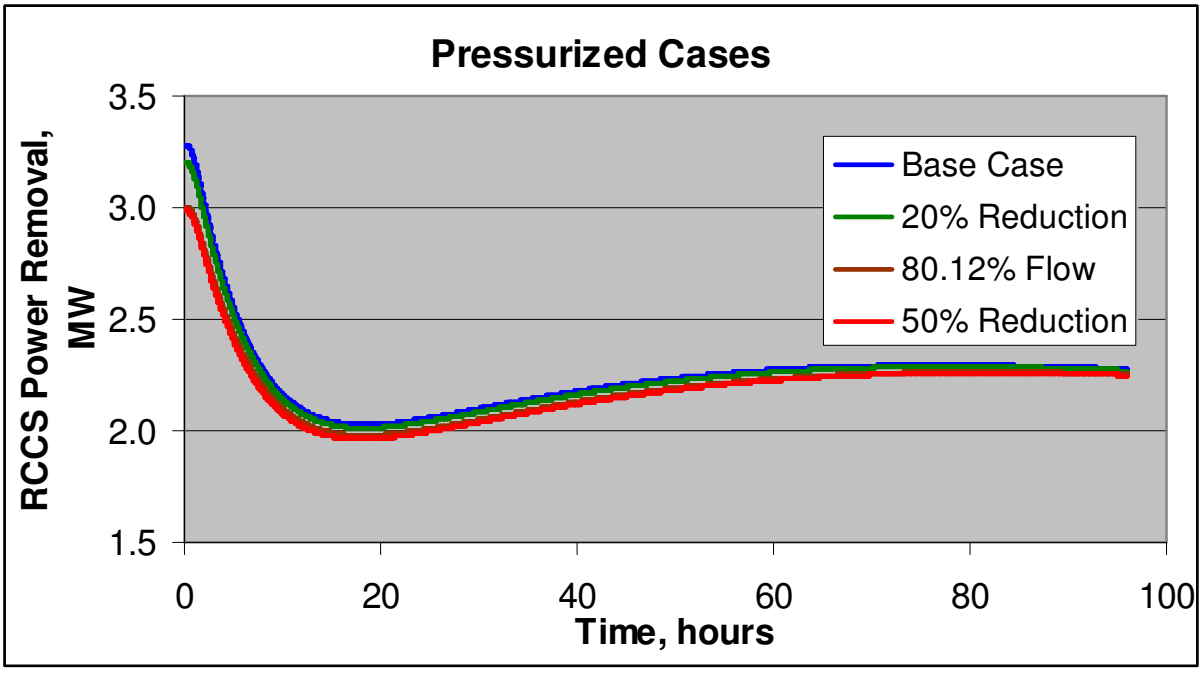

Figure 11. Effect of RCCS Film Coefficient and Initial Air Flow Rate on the RCCS Power Removal for the Pressurized Conduction

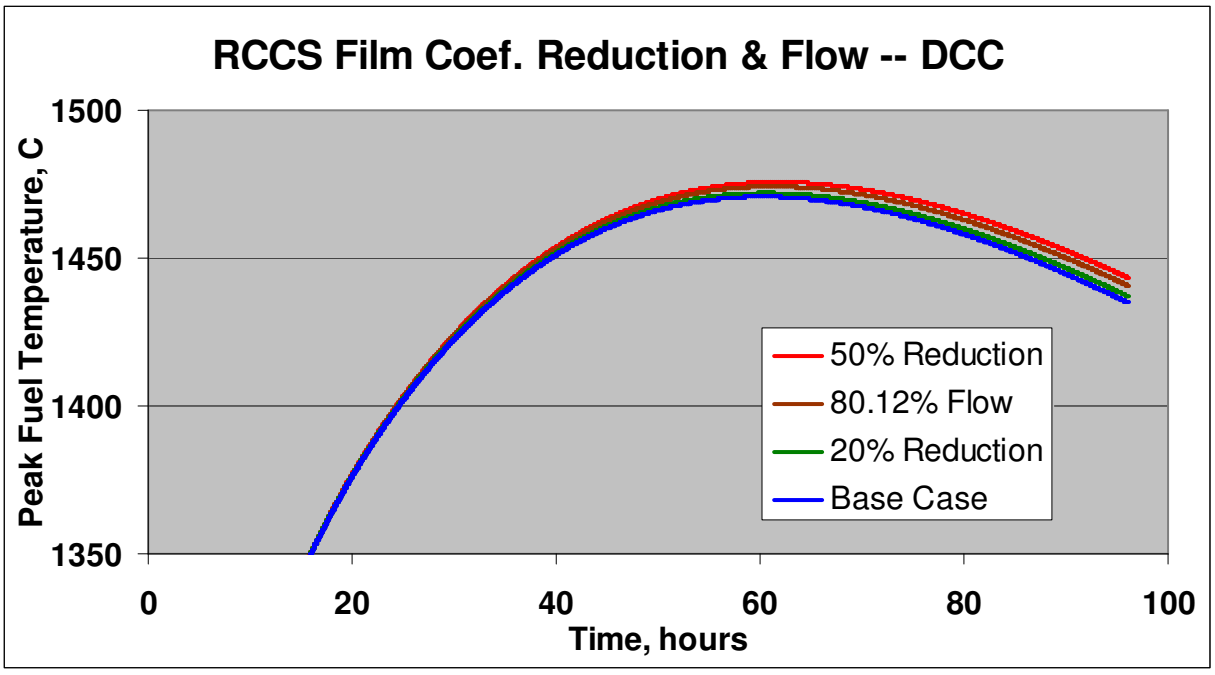

Figure 12. Effect of RCCS Film Coefficient and Initial Air Flow Rate on the Peak Fuel Temperature for the Depressurized Conduction Cooldown

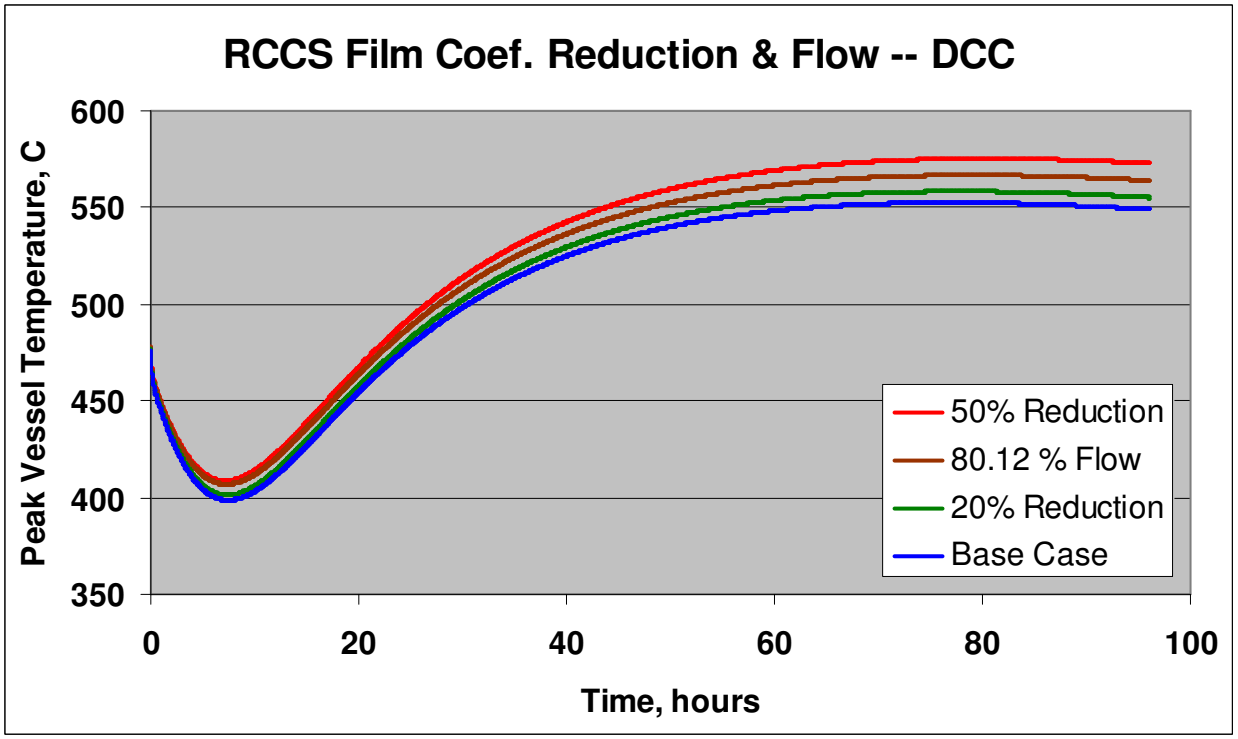

Figure 13. Effect of RCCS Film Coefficient and Initial Air Flow Rate on the Peak Reactor Vessel Temperature for the Depressurized Conduction Cooldown

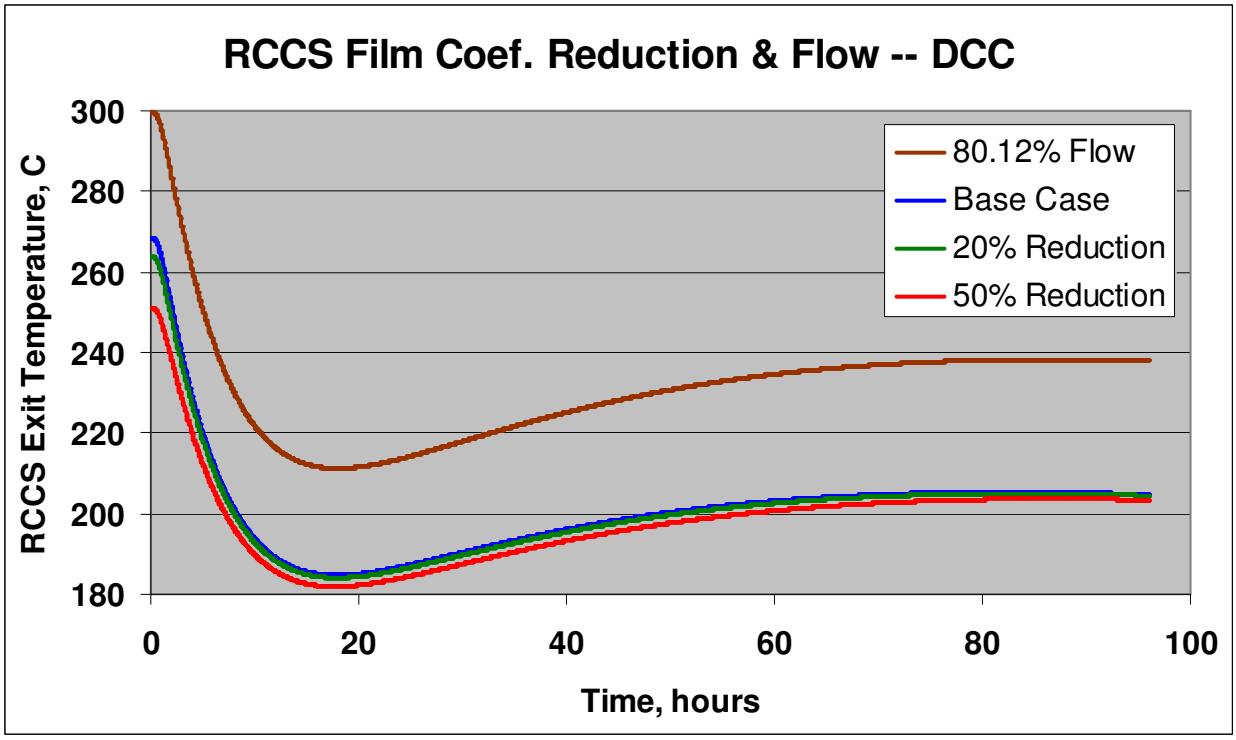

Figure 14. Effect of RCCS Film Coefficient and Initial Air Flow Rate on the RCCS Exit Coolant Temperature for the Depressurized Conduction Cooldown

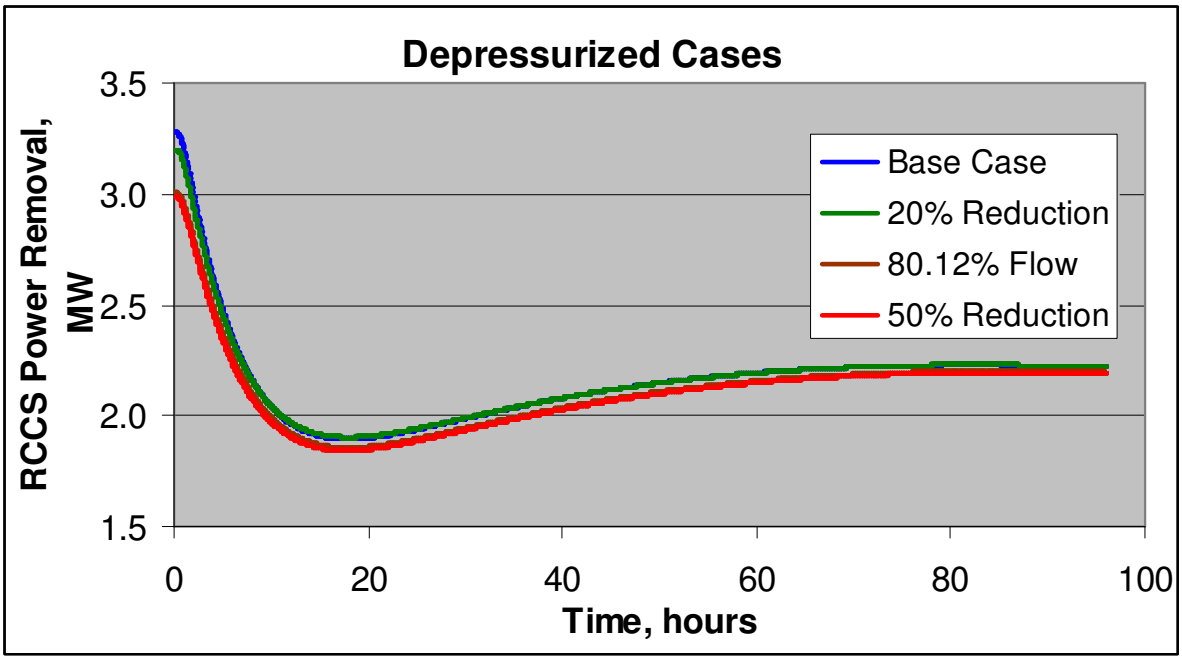

Figure 15. Effect of RCCS Film Coefficient and Initial Air Flow Rate on the RCCS Power Removal for the Depressurized Conduction

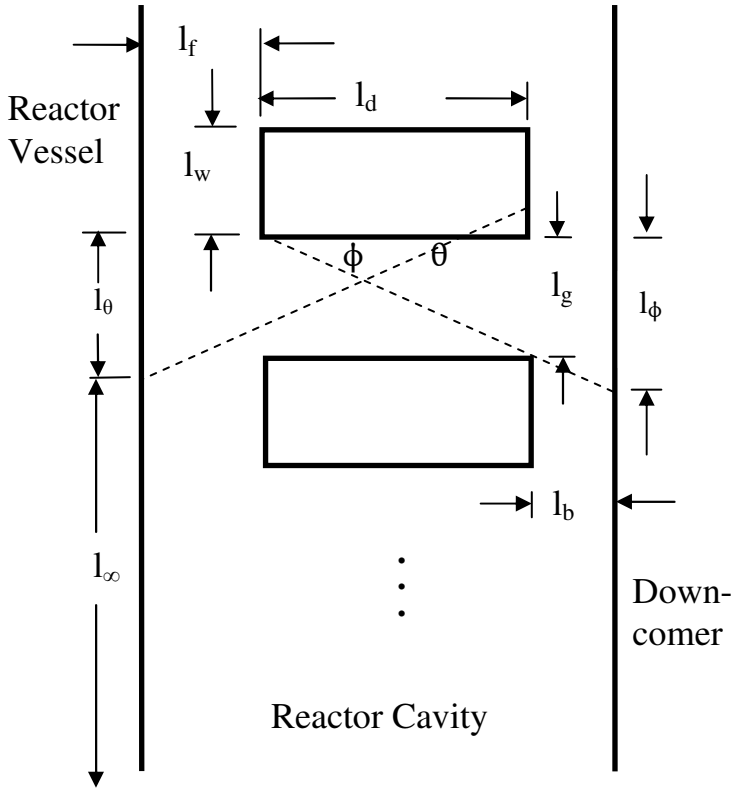

Figure 16 Dimensions of RCCS in Plan View

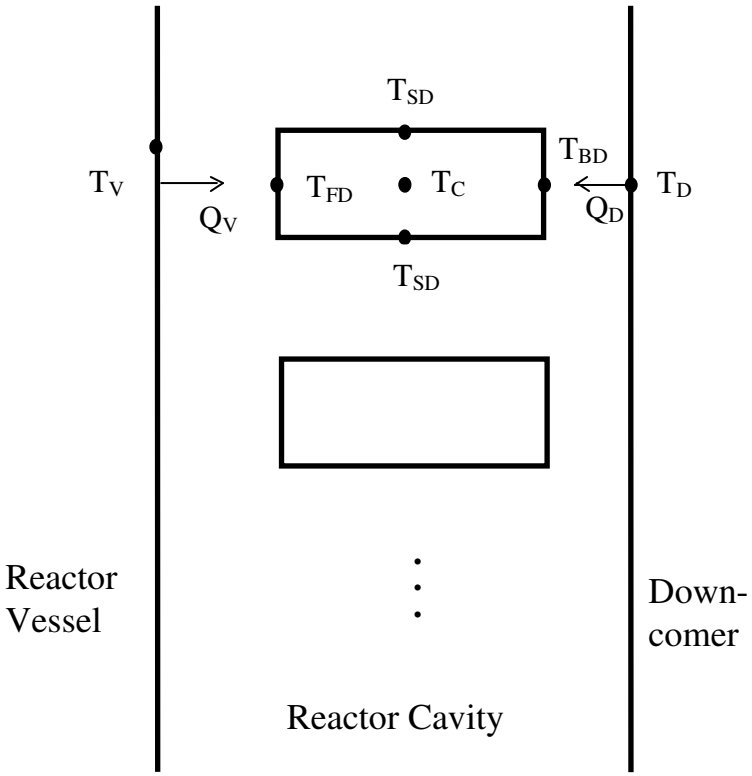

Figure 17 Variables in RCCS Radiation Model

Fig. 18 Definition of Elemental View Factors for Reactor Vessel to Side of Duct

Radiant Exchange Element	1 → A	2 → A	1+2 → A	2 → B	0 → B	0+2 → B	2 → 8
View Factor	F_{1A}	F_{2A}	F_{1+2A}	F_{2B}	F_{0B}	F_{0+2B}	F_{28}

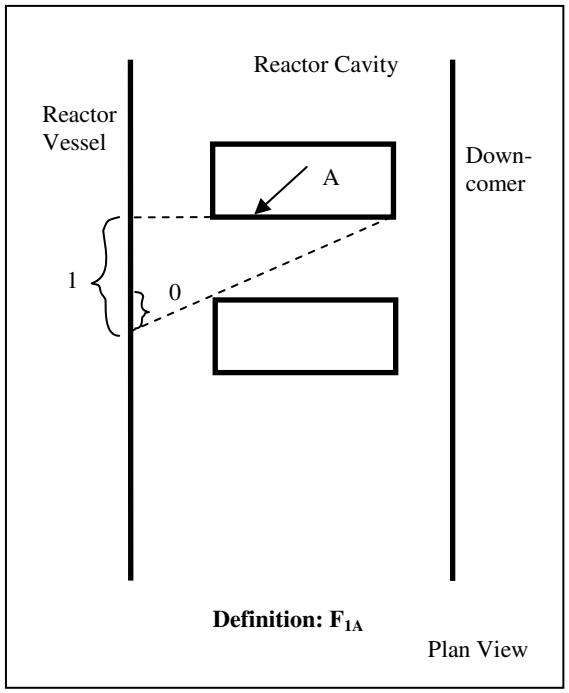

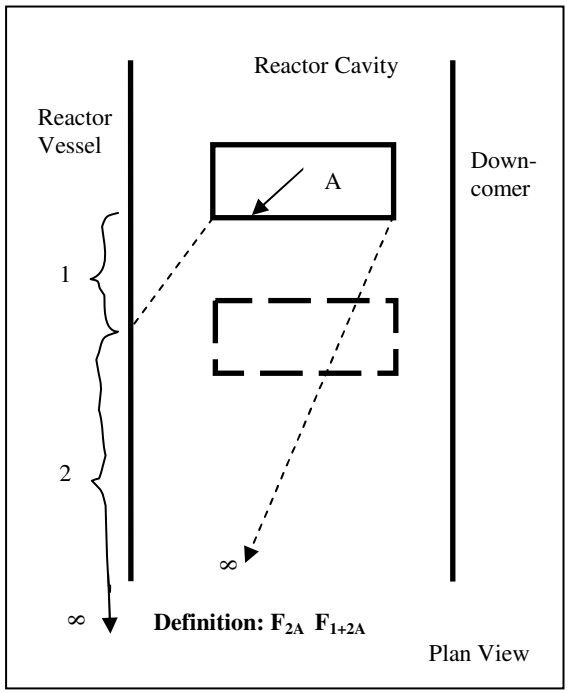

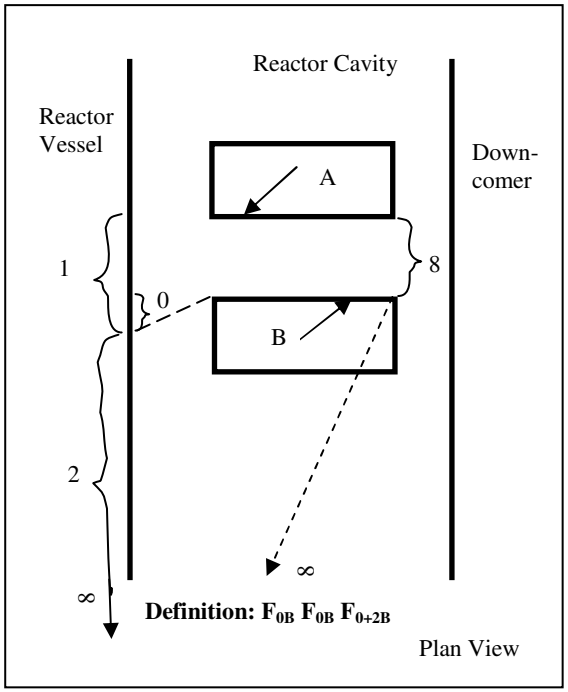

Fig. 19 Definition of Elemental View Factors for Side of Duct to Downcomer Wall

Radiant Exchange Element	A → 3	A → 4	A → 3+4	B → 4	B → 7	B → 4+7	9 → 4
View Factor	F_{A3}	F_{A4}	F_{A3+4}	F_{B4}	F_{B7}	F_{B4+7}	F_{94}

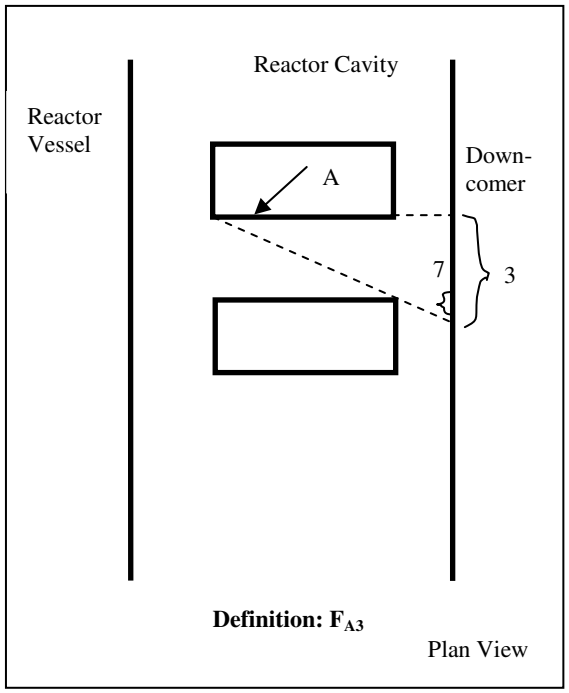

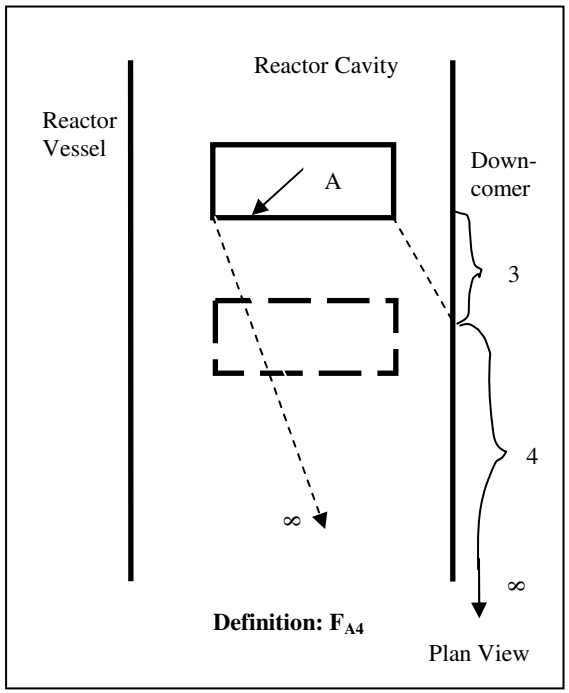

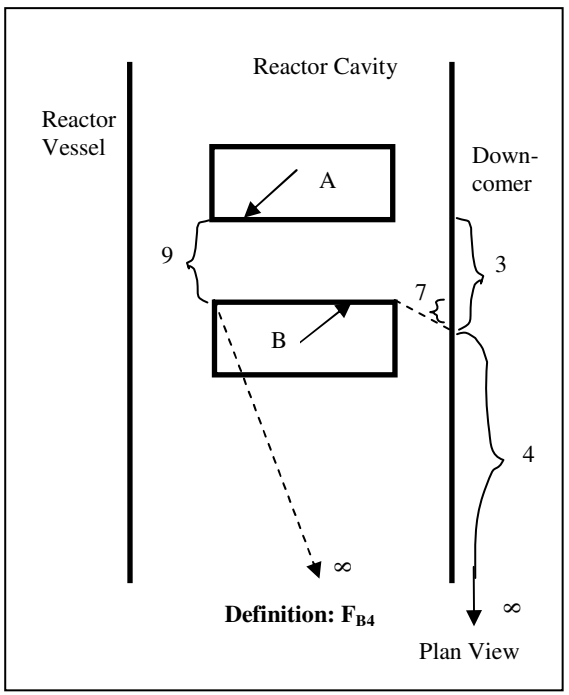

Fig. 20 Definition of Elemental View Factors for Vessel Wall to Front of Duct and Back of Duct to Downcomer Wall

Radiant Exchange Element	5 → C	D → 6
View Factor	F_{5C}	F_{D6}

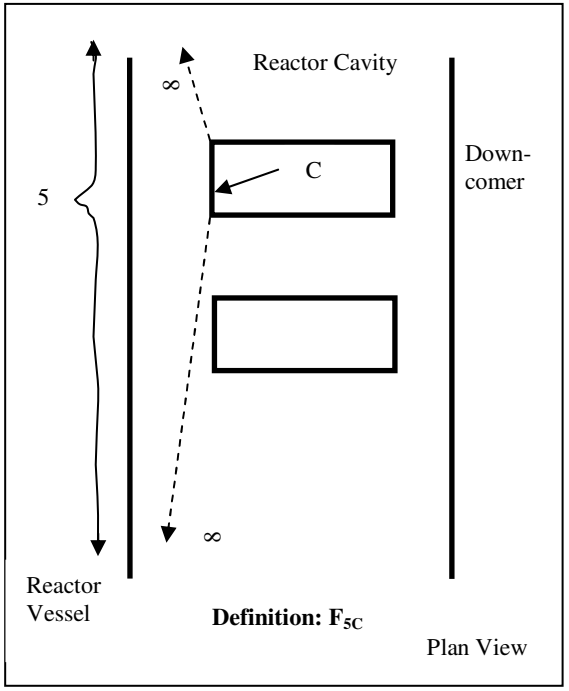

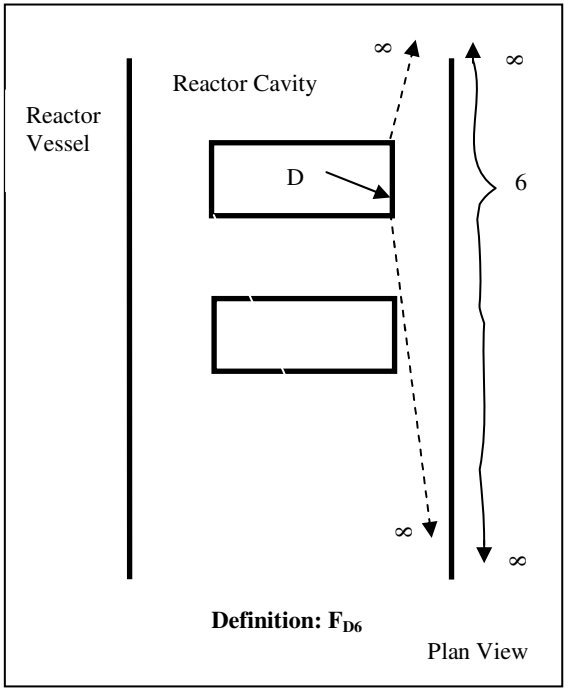

Fig. 21 Definition of Elemental View Factors for Interior Surfaces of Duct

Radiant Exchange Element	E → F	G → F	G → H
View Factor	F_{EF}	F_{GF}	F_{GH}

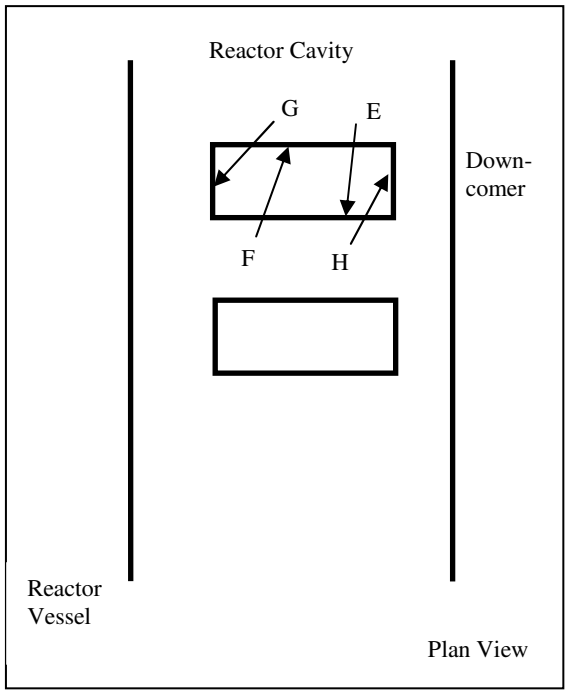

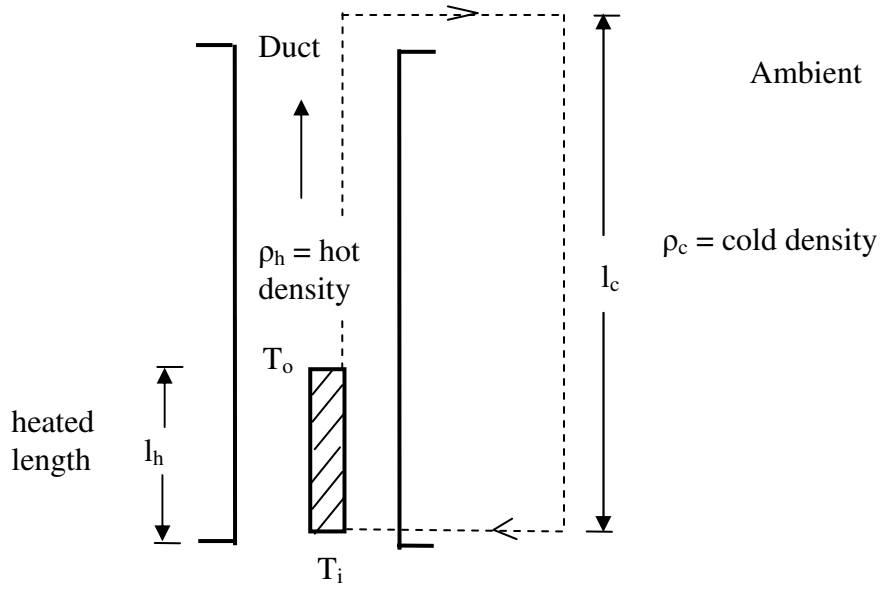

Figure 22 Simplified Representation of Duct Interior Natural Convection Circuit in RCCS

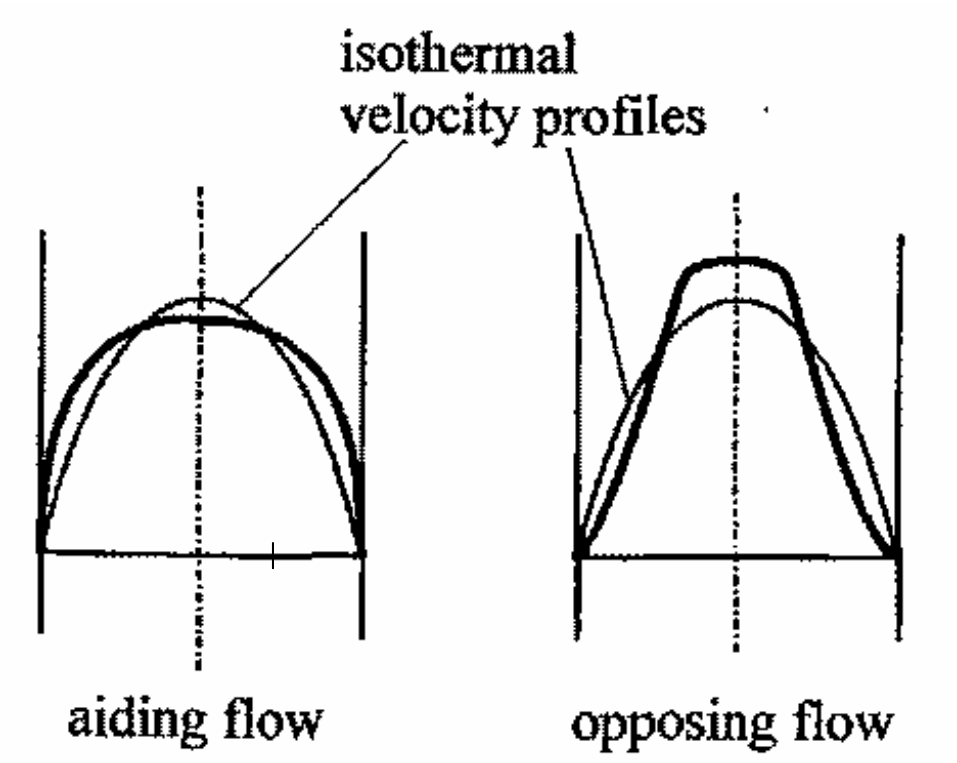

Figure 23. Velocity Profiles under Aiding and Opposing Turbulent Flow Conditions [11]

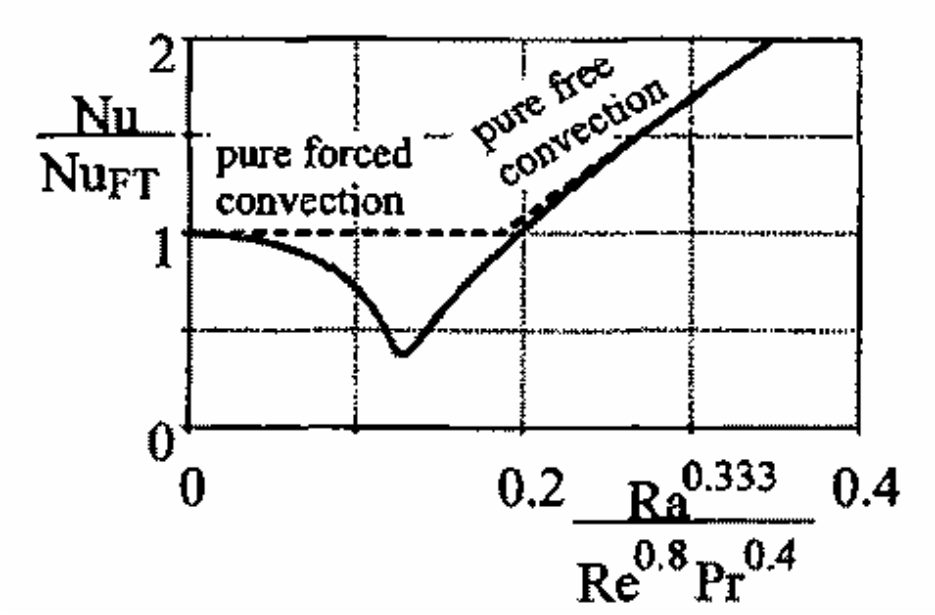

Figure 24. Heat Transfer for Aiding Mixed Convection [8]

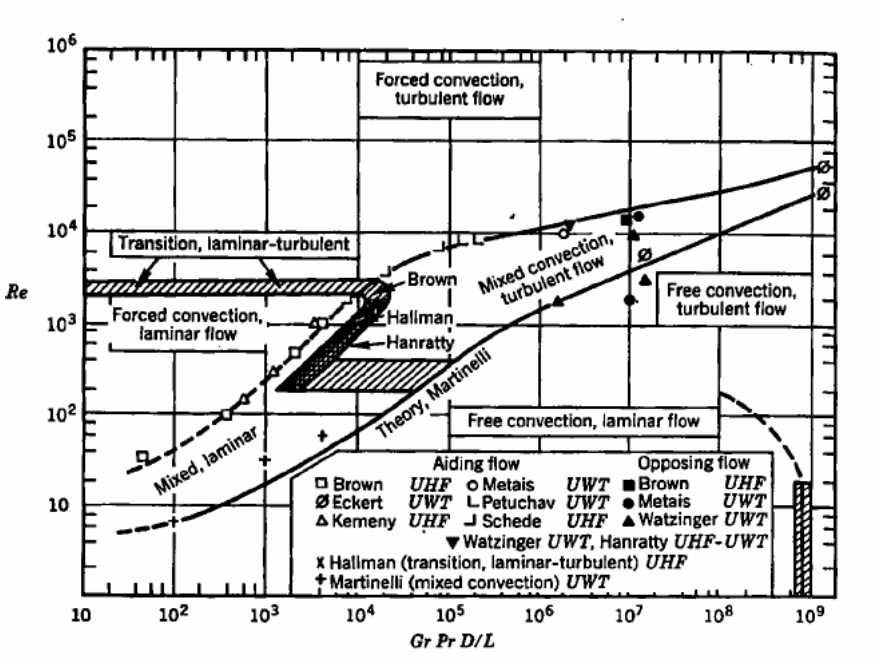

Fig. 25 Map Identifying Mixed Convection Regime [9]

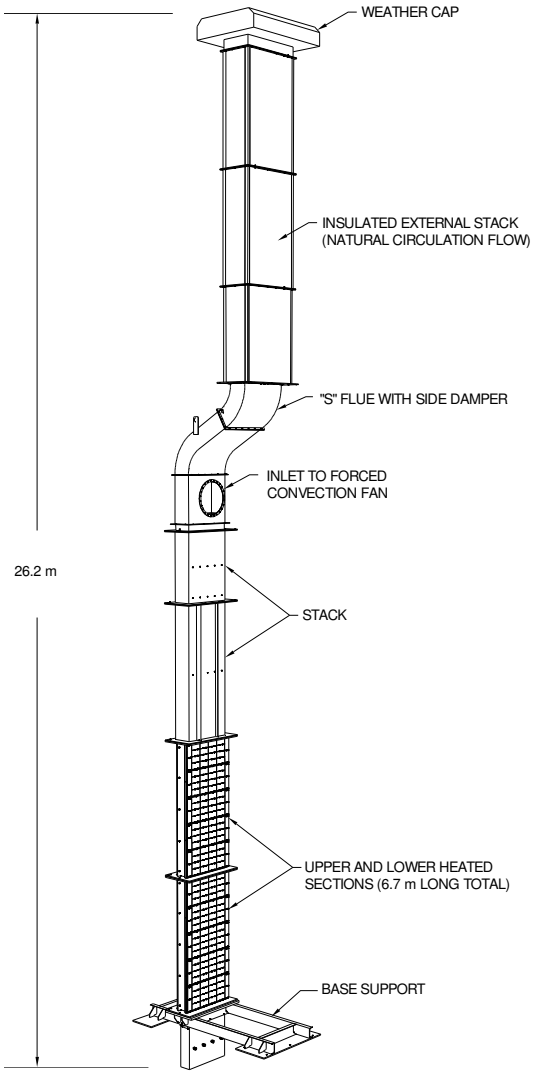

Fig. 26 Profile View of NSTF

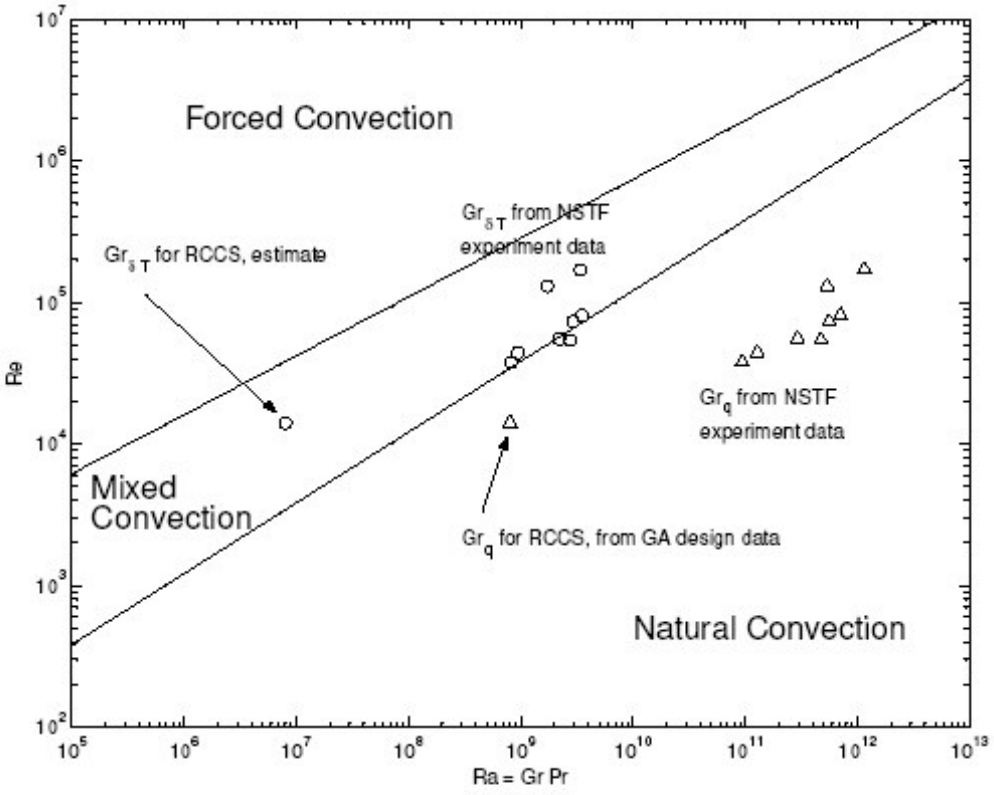

Fig. 27 Dimensionless Numbers for NSTF and RCCS Air Duct Plotted with respect to Convection Regions

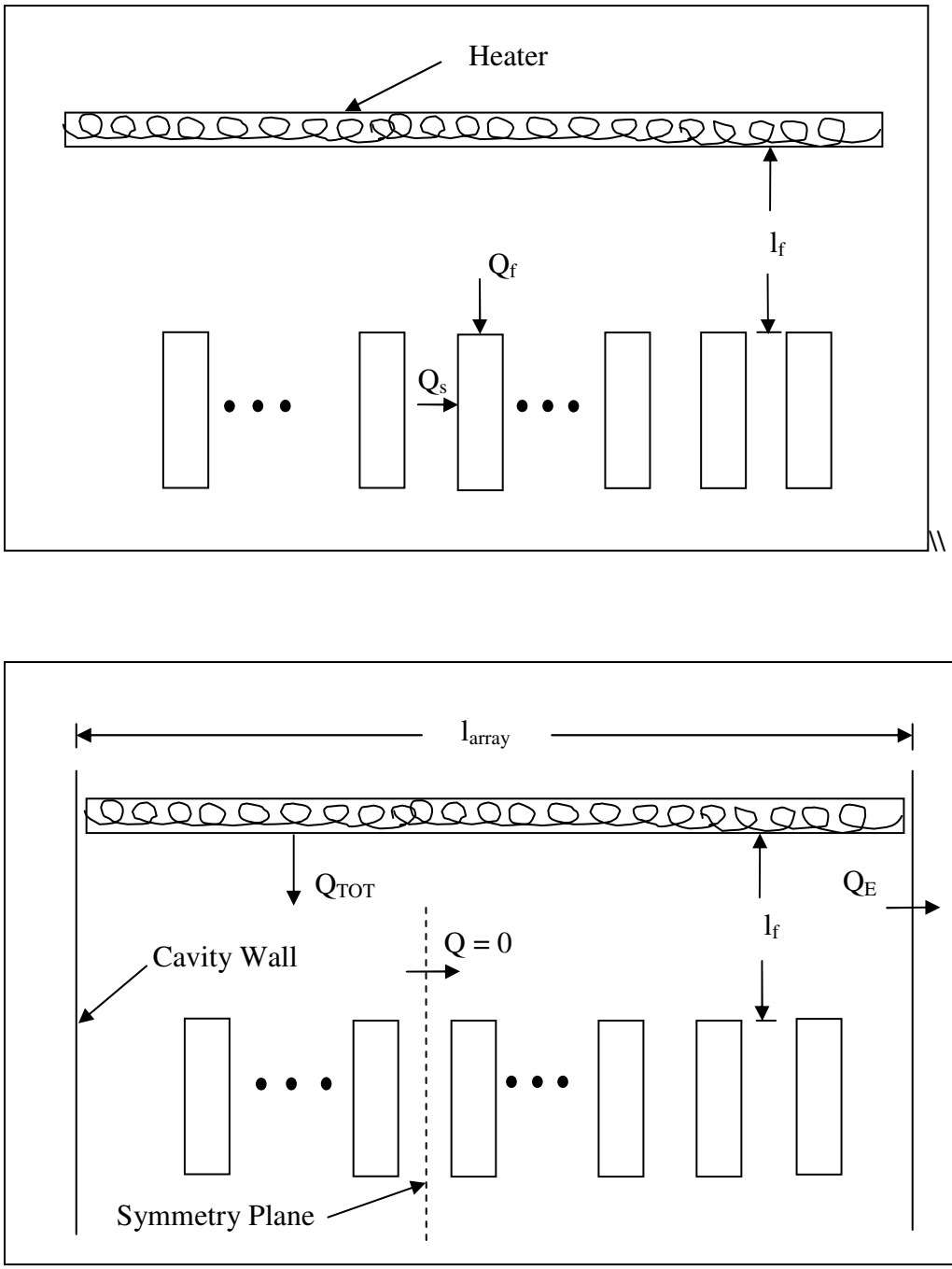

Figure 28 Variables Associated with Edge Losses in a Series of Ducts

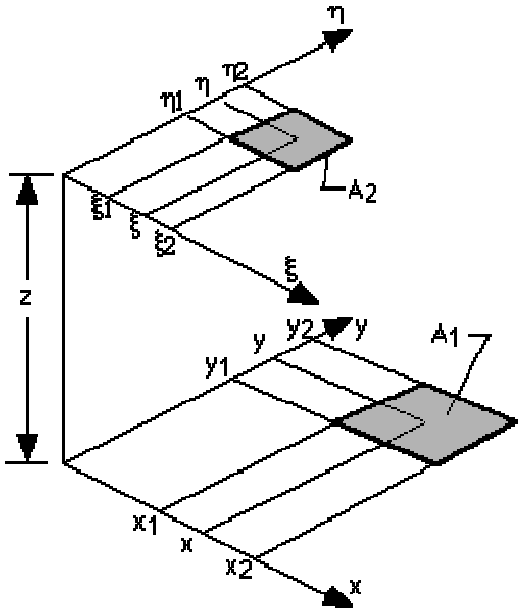

$$F_{1-2} = \frac{1}{(x_2 - x_1)(y_2 - y_1)} \sum_{l=1}^{2} \sum_{k=1}^{2} \sum_{j=1}^{2} \sum_{i=1}^{2} (-1)^{(i+j+k+l)} G(x_i, y_j, \eta_k, \xi_l)$$

$$G = \frac{1}{2\pi} \left(\begin{array}{l} (y-\eta)\left[(x-\xi)^2 + z^2\right]^{1/2} \tan^{-1}\left\{ \dfrac{y-\eta}{\left[(x-\xi)^2 + z^2\right]^{1/2}} \right\} \\ \quad + (x-\xi)\left[(y-\eta)^2 + z^2\right]^{1/2} \tan^{-1}\left\{ \dfrac{x-\xi}{\left[(y-\eta)^2 + z^2\right]^{1/2}} \right\} \\ \quad - \dfrac{z^2}{2} \ln\left[(x-\xi)^2 + (y-\eta)^2 + z^2\right] \end{array} \right)$$

Fig. 29 View Factor for Rectangle to Rectangle in a Parallel Plane. All boundaries are parallel or perpendicular to x and ξ boundaries. [J.R. Howell, http://www.me.utexas.edu/~howell]

Table 1. Relationship of Duty Cycle/Design Basis Events to Features of Asymptotic Steady-State Operating Regime

Values of Operating Regime Variables			Full Power Operation	Operational Transients	Refueling	Upsets													
						Protected							Unprotected						
						Loss of Generator Load	Reactivity Insertion	Loss of Cooling	Shaft Breakage	Loss of Coolant	Overcooling	Flow Blockage	Loss of Generator Load	Reactivity Insertion	Loss of Cooling	Shaft Breakage	Loss of Coolant	Overcooling	Flow Blockage
	Pressure	Normal Pressure	X	X		X	X	X	X		X	X	X	X	X	X	X		X	X
		Depressurized			X					X							X		
	Cooling	Forced Convection	X	X	X	X	X		X		X		X	X		X		X	
		Conduction						X		X		X			X		X		X
	Heating	Neutronic	X	X									X	X	X	X	X	X	X
		Decay Heat			X	X	X	X	X	X	X	X							

Table 2 Asymptotic Steady-State Operating Regimes and the Duty Cycle/Design Basis Events They Encompass. Ranked Generally in Order of Increasing Severity

Asymptotic Steady-State Operating Regime	Initiating Duty Cycle/Design Basis Events
OR1 - Normal Pressure/ Forced Convection Cooling/ Shutdown Decay Heat Generation	Loss of Generator Load - Protected Reactivity Insertion – Protected Shaft Breakage – Protected Overcooling - Protected
OR2 - Normal Pressure/ Forced Convection Cooling/ Neutronic Power	Full Power Operation. Operational Transients. Loss of Generator Load - Unprotected Reactivity Insertion – Unprotected Shaft Breakage – Unprotected Unprotected Overcooling - Unprotected
OR3 - Normal Pressure/ Conduction Cooling/ Shutdown Decay Heat	Loss of Cooling - Protected Flow Blockage - Protected
OR4 - Normal Pressure/ Conduction Cooling/ Neutronic Power	Loss of Cooling - Unprotected Flow Blockage - Unprotected
OR5 - Depressurized/ Forced Convection Cooling/ Shutdown Decay Heat	Refueling
OR6 - Depressurized/ Conduction Cooling/ Shutdown Decay Heat	Loss of Coolant - Protected
OR7 - Depressurized/ Conduction Cooling/ Neutronic Power	Loss of Coolant - Unprotected

Table 3
Peak Temperatures and RCCS Air Flow Rates for the Pressurized Conduction Cooldown

Configuration	Peak Temperature, C		RCCS Air Flow, kg/s	
(Case)	Fuel	Vessel	Maximum*	Minimum
Base Case	1317	513	14.13	13.11
80% RCCS Film Coefficient	1318	519	14.08	13.09
50% RCCS Film Coefficient	1323	535	13.94	13.01
80.12% Initial Air Flow	1322	528	11.36	10.79

*The initial value is the maximum value.

Table 4
Peak Temperatures and RCCS Air Flow Rates for the Depressurized Conduction Cooldown

Configuration	Peak Temperature, C		RCCS Air Flow, kg/s	
(Case)	Fuel	Vessel	Maximum*	Minimum
Base Case	1471	552	14.13	12.98
80% RCCS Film Coefficient	1472	558	14.08	12.95
50% RCCS Film Coefficient	1476	575	13.94	12.88
80.12% Initial Air Flow	1474	567	11.36	10.71

*The initial value is the maximum value.

Table 5 Composite View Factor Expressions for Reactor Cavity

Exchanging Pairs			View Factor Expression
Source	Destination	Subscript	
Reactor Vessel	Side of Duct	V-SD	$(l_\infty+l_\theta)F_{V\text{-}SD} = l_\theta F_{1A} + l_\infty F_{2A} - (l_\infty F_{2B} - l_\infty F_{28})$ (see Figure 28 for parallel plane view factors)
Side A of Duct	Side B of Duct	A-B	F_{AB}
Side of Duct	Downcomer	SD-D	$l_d F_{SD\text{-}D} = l_d (F_{A3} + F_{A4} - F_{B4}) + l_g F_{94}$ $= l_\phi F_{3A} + l_\infty F_{4A} - l_\infty F_{4B} + l_g F_{94}$ (see Figure 28 for parallel plane view factors)
Reactor Vessel	Front of Duct	V-FD	$F_{V\text{-}FD} = F_{5C}$
Back of Duct	Downcomer	BD-D	$F_{BD\text{-}D} = F_{D6}$
Reactor Vessel	Downcomer	V-D	$F_{V\text{-}D} = 1 - F_{V\text{-}FD} - 2F_{V\text{-}SD}$

Table 6 Composite Reverse View Factor Expressions for Reactor Cavity

Exchanging Pairs			View Factor Expression
Source	Destination	Subscript	
Side of Duct	Reactor Vessel	SD-V	$l_d F_{SD\text{-}V} = (F_{A1} + F_{A2}) l_d - F_{B2} l_d + l_g F_{82} = l_\theta F_{1A} + l_\infty F_{2A} - F_{2B} l_\infty + l_\infty F_{28} = (l_\infty + l_\theta) F_{V\text{-}SD}$
Side B of Duct	Side A of Duct	B-A	$F_{BA} = F_{AB}$
Downcomer	Side of Duct	D-SD	$(l_\infty + l_\phi) F_{D\text{-}SD} = l_\phi F_{3A} + l_\infty F_{4A} - l_\infty F_{4B} + l_\infty F_{49} = l_\phi F_{3A} + l_\infty F_{4A} - l_\infty F_{4B} + l_g F_{94}$
Front of Duct	Reactor Vessel	FD-V	$F_{FD-V} = \frac{2(l_\infty + l_\theta) + l_W}{l_W} F_{V-FD}$
Downcomer	Back of Duct	D-BD	$F_{D-BD} = \frac{l_W}{2(l_\infty + l_\theta) + l_W} F_{BD-D}$
Downcomer	Reactor Vessel	D-V	$F_{D\text{-}V} = 1 - F_{D\text{-}BD} - 2F_{D-SD}$

Table 7 Elemental View Factor Expressions

Exchanging Surfaces		Area per Unit Length * View Factor
Source	Destination	
1	A	$F_{lA}(l_\theta, l_f + l_d, l_f) = \frac{1}{2}\left[\frac{l_f + l_d}{l_\theta} - \left(1 + \left[\frac{l_f + l_d}{l_\theta}\right]^2\right)^{\frac{1}{2}} - \frac{l_f}{l_\theta} + \left(1 + \left[\frac{l_f}{l_\theta}\right]^2\right)^{\frac{1}{2}}\right]$, $\theta = \tan^{-1}\left(\frac{l_g}{l_d}\right)$, $l_\theta = (l_f + l_d)\tan\theta$
2	A	$l_\infty F_{2A} = (l_\theta + l_\infty) F_{1+2A} - l_\theta F_{1A}$
1+2	A	$F_{lA}(l_\theta + l_\infty, l_f + l_d, l_f)$
2	B	$l_\infty F_{2B} = (l_\theta - l_g + l_\infty) F_{0+2B} - (l_\theta - l_g) F_{0B}$
0	B	$F_{lA}(l_\theta - l_g, l_f + l_d, l_f)$
0+2	B	$F_{lA}(l_\theta - l_g + l_\infty, l_f + l_d, l_f)$
2	8	$l_\infty F_{28} = l_g F_{82}$ [see Figure 7 for F_{82}]

Table 7 Elemental View Factor Expressions (continued)

Exchanging Surfaces		Area per Unit Length * View Factor
Source	Destination	
A	3	$F_{A3}(l_\varphi, l_d + l_b, l_b) = \frac{1}{2}\left[1 + \frac{l_\varphi}{l_d + l_b} - \left(1 + \left[\frac{l_\varphi}{l_d + l_b}\right]^2\right)^{\frac{1}{2}}\right] - \frac{1}{2}\left[1 + \frac{l_\varphi}{l_b} - \left(1 + \left[\frac{l_\varphi}{l_b}\right]^2\right)^{\frac{1}{2}}\right]$ $\varphi = \tan^{-1}\left(\frac{l_g}{l_d}\right)$, $l_\varphi = (l_b + l_d)\tan\varphi$
A	4	$F_{A4} = F_{A3+4} - F_{A3}$
A	3+4	$F_{A3+4} = F_{A3}(l_\varphi + l_\infty, l_d + l_b, l_b)$
B	4	$F_{B4} = F_{B4+7} - F_{B7}$
B	7	$F_{B7} = F_{A3}(l_\varphi - l_g, l_d + l_b, l_b)$
B	4+7	$F_{B4+7} = F_{A3}(l_\varphi - l_g + l_\infty, l_d + l_b, l_b)$
9	4	$l_g F_{94}$ [see Fig. 7 for F_{94}]

Table 7 Elemental View Factor Expressions (continued)

5	C	$(2\,(l_{\infty}+l_{\theta})+l_{w})\,F_{5C}=\frac{l_f}{2}\left[\left(\left(\frac{2(l_{\infty}+l_{\theta}+l_{w})}{l_f}\right)^2+4\right)^{\frac{1}{2}}-\left(\left(\frac{2\,(l_{\infty}+l_{\theta})}{l_f}\right)^2+4\right)^{\frac{1}{2}}\right]$
D	6	$l_w\,F_{D6}=\frac{l_b}{2}\left[\left(\left(\frac{2(l_{\infty}+l_{\theta}+l_{w})}{l_b}\right)^2+4\right)^{\frac{1}{2}}-\left(\left(\frac{2\,(l_{\infty}+l_{\theta})}{l_b}\right)^2+4\right)^{\frac{1}{2}}\right]$
A	B	

Table 8 Composite View Factor Expressions for Interior Surfaces of Duct

Exchanging Pairs			View Factor Expression
Source	Destination	Subscript	
Front of Duct Interior	Side of Duct Interior	FDI-SDI	$F_{FDI-SDI} = F_{GF}$
Front of Duct Interior	Back of Duct Interior	FDI-BDI	$F_{FDI-BDI} = F_{GH}$
Side E of Duct Interior	Side F of Duct Interior	SDI-SDI	$F_{SDI-SDI} = F_{EF}$
Side of Duct Interior	Back of Duct Interior	SDI- BDI	$l_d F_{SDI- BDI} = l_d F_{FH} = l_w F_{GF}$
Side of Duct Interior	Front of Duct Interior	SDI- FDI	$l_d F_{SDI- FDI} = l_w F_{GF}$
Back of Duct Interior	Side of Duct Interior	BDI-SDI	$l_w F_{BDI-SDI} = l_d F_{FH} = l_w F_{GF}$
Back of Duct Interior	Front of Duct Interior	BDI- FDI	$F_{BDI- FDI} = F_{GH}$

Table 9 Elemental View Factor Expressions for Interior Surfaces of Duct

Exchanging Surfaces		Area per Unit Length * View Factor
Source	Destination	
E	F	$l_d F_{EF} = l_w \left[\left(\left(\frac{l_d}{l_w} \right)^2 + 1 \right)^{\frac{1}{2}} - 1 \right]$
G	F	$F_{GF} = \frac{1}{2} \left[1 + \frac{l_d}{l_w} - \left(1 + \left[\frac{l_d}{l_w} \right]^2 \right)^{\frac{1}{2}} \right]$
G	H	$l_w F_{GH} = l_d \left[\left(\left(\frac{l_w}{l_d} \right)^2 + 1 \right)^{\frac{1}{2}} - 1 \right]$

Table 10 Magnitude of Individual Terms in Momentum Equation

Gravity, Pa	$gh(\rho_{out} - \rho_{in}) = gh\rho_{in}\,\beta\Delta T$	$9.8 \cdot 26 \cdot 0.83 \cdot 0.0023 \cdot 225 = 108$	
Acceleration, Pa	$\frac{W^2}{A^2}\left(\frac{1}{\rho_{out}} - \frac{1}{\rho_{in}}\right) = \frac{W^2}{\rho_{in} A^2}\left(\frac{1}{1-\beta\Delta T} - 1\right)$	$\frac{0.049^2}{0.83 \cdot (0.05 \cdot 0.25)^2}\left(\frac{1}{1 - 0.0023 \cdot 225} - 1\right) = 20$	Sum=133
Friction, Pa	$4f\,\frac{l_c}{D_h}\,\rho\frac{v^2}{2} = 4f\,\frac{l_c}{D_h}\,\frac{1}{2\rho}\left(\frac{W}{A}\right)^2, f = \frac{0.079}{Re^{0.25}}$	$\frac{4 \cdot 0.079}{14{,}000^{0.25}}\,\frac{34}{0.083 \cdot 2 \cdot 0.83}\left(\frac{0.049}{0.05 \cdot 0.25}\right)^2 = 109$	
Entrance and Exit Loss, Pa	$2\,K\frac{1}{2\rho}\left(\frac{W}{A}\right)^2$	$\frac{0.2}{0.83}\left(\frac{0.049}{0.05 \cdot 0.25}\right)^2 = 4$	

Table 11 Data Used in Calculation of Individual Terms in Momentum Equation

A (m^2)	W (kg/s)	ΔT (C)	ρ (kg/m^3)	l_h (m)	B (1/C)	l_c (m)	$h = l_c - 1/2 l_h$ (m)	D_h (m)
0.05*0.25	0.049	225	0.83	16	0.0023	34	26	0.083

Table 12 Dimensionless Numbers for Unfinned Experiments in NSTF

Date	Re	q'' (w/m^2-s)	Bulk T (C)	μ (μPa-s)	k (W/m-K)	C_p (J/kg-K)	Pr	δT	$Gr_{\delta T} = \frac{g\rho^2 \beta q \delta T D^3}{\mu^2}$	$Gr_{q''} = \frac{g\rho^2 \beta q'' D^4}{k\mu^2}$
1-28-87	55000	1900	29	17.5	0.027	1000	0.60	291	2.2e9	0.42e12
2-23-87	130000	3500	30	17.5	0.027	1000	0.60	235	1.7e9	0.77e12
3-25-87	170000	8500	40	18.3	0.028	1000	0.62	484	3.4e9	1.60e12
9-10-87	80800	7200	70	20.8	0.030	1000	0.69	662	3.5e9	1.00e12
10-1-87	44000	830	30	17.5	0.027	1000	0.60	142	0.9e9	0.18e12
10-7-87	73000	5000	58	19.8	0.029	1000	0.66	507	2.9e9	0.80e12
10-8-97	54000	4300	62	20.0	0.029	1000	0.66	494	2.8e9	0.67e12
10-12-87	37700	690	38	18.3	0.028	1000	0.62	145	0.8e9	0.13e12

* $g = 9.8\ m/s^2$, $\rho = 1.16\ kg/m^3$, $\beta = 0.0023\ 1/K$, D = 4*12*52/(2*(12+52))*2.54e-02 = 0.50 m

Table 13 RCCS Duct Dimensions and Thermal-Hydraulic Conditions at Reactor Full Power

Parameter	Value
RCCS Power*, Q (Mwt)	3.3
RCCS Air Mass Flowrate *, W (kg/s)	14.3
Number of Ducts*, n	292
Average Duct Air Flowrate , w (kg/s)	0.049
Duct Dimensions*, a=horizontal width of heat transfer surface x b=horizontal depth (m)	0.05 x 0.25
Hydraulic Diameter, D (m)	0.083
Length of Active Core Region, L (m)	7.93
Duct Wall Heat Flux, (Mw/m^2) $q'' = Q/(naL)$	0.029

* from [7].

Table 14 RCCS Duct Coolant Hydraulic Conditions at Reactor Full Power

Duct Air Flowrate (kg/s)	Pressure (MPa)	Average Bulk Temperature (C)	Viscosity (μPa-s)	$Re = \frac{wD}{\mu A}$
0.049	0.1	(43+274)/2 =159	23	14,000

Table 15 RCCS Duct Coolant Thermal Conditions at Reactor Full Power

Pressure (MPa)	Average Bulk Temperature (C/K)	Wall Heat Flux, q" (Mw/m^2)	Density, ρ (kg/m^3)	Coefficient of Volumetric Thermal Expansion, β (1/K)	Viscosity, μ (μPa-s)	Thermal Conductivity, k (W/m-K)	$Gr_{q''} = \frac{g\rho^2 \beta q'' D^4}{k\mu^2}$
0.1	159/432	0.029	0.83	0.0023	23	0.035	1.15×10^9

Table 16 Dimensions and View Factors for Representative Air Duct in NSTF

l_d (cm)	l_w (cm)	l_g (cm)	l_f (cm)	l_b (cm)	$F_{V\text{-}FD}$ Eq. (6a)	$F_{V\text{-}SD}$ Eq. (6b)
10	2	2	4	4	0.5000	0.4645

Nuclear Engineering Division
Argonne National Laboratory
9700 South Cass Avenue, Bldg. 208
Argonne, IL 60439-4842

www.anl.gov

A U.S. Department of Energy laboratory managed by UChicago Argonne, LLC